The Astrophysical Journal, 898:107 (36pp), 2020 August 1 https://doi.org/10.3847/1538-4357/ab9f3a

ALMA Survey of Orion Planck Galactic Cold Clumps (ALMASOP). I. Detection of New Hot Corinos with the ACA

Shih-Ying Hsu[1,2], Sheng-Yuan Liu[2], Tie Liu[3], Dipen Sahu[2], Naomi Hirano[2], Chin-Fei Lee[2], Ken'ichi Tatematsu[4,5], Gwanjeong Kim[4], Mika Juvela[6], Patricio Sanhueza[7], Jinhua He[8,9,10], Doug Johnstone[11,12], Sheng-Li Qin[13], Leonardo Bronfman[10], Huei-Ru Vivien Chen[14], Somnath Dutta[2], David J. Eden[15], Kai-Syun Jhan[1,2], Kee-Tae Kim[16,17], Yi-Jehng Kuan[2,18], Woojin Kwon[19,16], Chang Won Lee[16,17], Jeong-Eun Lee[20], Anthony Moraghan[2], M. G. Rawlings[21], Hsien Shang[2], Archana Soam[22], M. A. Thompson[23], Alessio Traficante[24], Yuefang Wu[25,26], Yao-Lun Yang[27], and Qizhou Zhang[28]

[1] National Taiwan University, No. 1, Sec. 4, Roosevelt Rd., Taipei 10617, Taiwan (R.O.C.); seansyhsu@gmail.com
[2] Institute of Astronomy and Astrophysics, Academic Sinica, 11F of Astronomy-Mathematics Building, AS/NTU, No.1, Sec. 4, Roosevelt Rd, Taipei 10617, Taiwan (R.O.C.); syliu@asiaa.sinica.edu.tw
[3] Key Laboratory for Research in Galaxies and Cosmology, Shanghai Astronomical Observatory, Chinese Academy of Sciences, 80 Nandan Road, Shanghai 200030, People's Republic of China
[4] Nobeyama Radio Observatory, National Astronomical Observatory of Japan, National Institutes of Natural Sciences, 462-2 Nobeyama, Minamimaki, Minamisaku, Nagano 384-1305, Japan
[5] Department of Astronomical Science, SOKENDAI (The Graduate University for Advanced Studies), 2-21-1 Osawa, Mitaka, Tokyo 181-8588, Japan
[6] Department of Physics, P.O.Box 64, FI-00014, University of Helsinki, Finland
[7] National Astronomical Observatory of Japan, National Institutes of Natural Sciences, 2-21-1 Osawa, Mitaka, Tokyo 181-8588, Japan
[8] Yunnan Observatories, Chinese Academy of Sciences, 396 Yangfangwang, Guandu District, Kunming, 650216, People's Republic of China
[9] Chinese Academy of Sciences South America Center for Astronomy, National Astronomical Observatories, CAS, Beijing 100101, People's Republic of China
[10] Departamento de Astronomía, Universidad de Chile, Casilla 36-D, Santiago, Chile
[11] NRC Herzberg Astronomy and Astrophysics, 5071 West Saanich Rd, Victoria, BC, V9E 2E7, Canada
[12] Department of Physics and Astronomy, University of Victoria, Victoria, BC, V8P 5C2, Canada
[13] Department of Astronomy, Yunnan University, and Key Laboratory of Astroparticle Physics of Yunnan Province, Kunming 650091, People's Republic of China
[14] Institute of Astronomy and Department of Physics, National Tsing Hua University, Hsinchu 30013, Taiwan
[15] Astrophysics Research Institute, Liverpool John Moores University, iC2, Liverpool Science Park, 146 Brownlow Hill, Liverpool, L3 5RF, UK
[16] Korea Astronomy and Space Science Institute (KASI), 776 Daedeokdae-ro, Yuseong-gu, Daejeon 34055, Republic of Korea
[17] University of Science and Technology, Korea (UST), 217 Gajeong-ro, Yuseong-gu, Daejeon 34113, Republic of Korea
[18] Department of Earth Sciences, National Taiwan Normal University, Taipei, Taiwan (R.O.C.)
[19] Department of Earth Science Education, Seoul National University (SNU), 1 Gwanak-ro, Gwanak-gu, Seoul 08826, Republic of Korea
[20] School of Space Research, Kyung Hee University, 1732, Deogyeong-Daero, Giheung-gu Yongin-shi, Gyunggi-do 17104, Republic of Korea
[21] East Asian Observatory, 660 N. A'ohōkū Place, University Park, Hilo, HI 96720, USA
[22] SOFIA Science Center, USRA, NASA Ames Research Center, M.S.-12, N232, Moffett Field, CA 94035, USA
[23] Centre for Astrophysics Research, School of Physics Astronomy & Mathematics, University of Hertfordshire, College Lane, Hatfield, AL10 9AB, UK
[24] INAF-IAPS, via Fosso del Cavaliere, 100. I-00133, Rome, Italy
[25] Department of Astronomy, School of Physics, Peking University, Beijing, 1000871, People's Republic of China
[26] Kavli Institute for Astronomy and Astrophysics, Peking University, Beijing, 100871, People's Republic of China
[27] Department of Astronomy, University of Virginia, Charlottesville, VA 22904, USA
[28] Center for Astrophysics | Harvard & Smithsonian, 60 Garden Street, Cambridge, MA 02138, USA
Received 2020 March 9; revised 2020 June 19; accepted 2020 June 19; published 2020 July 29

Abstract

We report the detection of four new hot corino sources, G211.47–19.27S, G208.68–19.20N1, G210.49–19.79W, and G192.12–11.10, from a survey study of Planck Galactic Cold Clumps in the Orion Molecular Cloud Complex with the Atacama Compact Array. Three sources had been identified as low-mass Class 0 protostars in the Herschel Orion Protostar Survey. One source in the λ Orionis region is first reported as a protostellar core. We have observed abundant complex organic molecules (COMs), primarily methanol but also other oxygen-bearing COMs (in G211.47–19.27S and G208.68–19.20N1) and the molecule of prebiotic interest NH_2CHO (in G211.47–19.27S), signifying the presence of hot corinos. While our spatial resolution is not sufficient to resolve most of the molecular emission structure, the large line width and high rotational temperature of COMs suggest that they likely reside in the hotter and innermost region immediately surrounding the protostar. In G211.47–19.27S, the D/H ratio of methanol ($[CH_2DOH]/[CH_3OH]$) and the $^{12}C/^{13}C$ ratio of methanol ($[CH_3OH]/[^{13}CH_3OH]$) are comparable to those of other hot corinos. Hydrocarbons and long-carbon-chain molecules such as c-C_3H_2 and HCCCN are also detected in the four sources, likely tracing the outer and cooler molecular envelopes.

Unified Astronomy Thesaurus concepts: Astrochemistry (75); Interstellar molecules (849); Star forming regions (1565); Low mass stars (2050); Protostars (1302)

1. Introduction

Many Class 0/I low (and also intermediate) mass protostellar cores show considerable chemical diversity. Those cores, characterized by the presence of abundant saturated complex organic molecules (COMs) within a warm (~100 K) and compact (<100 au) region around the central protostar, are called "hot corinos" (Ceccarelli 2004). Hot corinos seem qualitatively similar to "hot cores," also characterized by abundant COMs, but are associated with larger (~1000 au) and warmer (~300 K) regions in high-mass star formation sites;

however, the abundances of the COMs in hot corinos can be, in some cases, orders of magnitude higher (fractional abundance with respect to the hydrogen molecule $X \sim 10^{-7} - 10^{-9}$) than those in hot cores (Ospina-Zamudio et al. 2018).

The current hot corino formation scenario can be described by three phases (Herbst & van Dishoeck 2009). Initially, atoms and molecules in the gas phase of prestellar cores accrete onto dust grains, and the zeroth-generation COMs (e.g., the COM precursor H_2CO, methanol CH_3OH, and possibly other COMs) are produced by grain surface chemistry during this "cold phase." In the "warm-up phase," the photodissociated radicals (e.g., methoxy radical CH_3O and formyl radical HCO of CH_3OH and H_2CO) form larger, complex molecules (e.g., methyl formate $HCOOCH_3$ and formic acid HCOOH) as the first-generation molecules via radical–radical reactions in the ice mantles. The "hot corino phase" takes place when the temperature reaches ∼100 K from 10 K in the cold phase. The icy mantles completely sublimate into the gas, and the second-generation molecules are consequently produced via gas-phase reactions.

So far, a good number of hot corinos have been identified, including IRAS 16293–2422 in the Rho Ophiuchi cloud complex (Cazaux et al. 2003); IRAS4A2, IRAS2A, IRAS4B, and SVS13-A in the Perseus molecular cloud (Bottinelli et al. 2004, 2007; Jorgensen et al. 2005; López-Sepulcre et al. 2017; Bianchi et al. 2018); B335 in Lynd L663 (Imai et al. 2016); B1b in Barnard 1 (Lefloch et al. 2018); Cep E-mm in the Cepheus E molecular cloud (Ospina-Zamudio et al. 2018); L483 in the Serpens-Aquila Rift (Oya et al. 2017; Jacobsen et al. 2019); Ser-emb 1, Ser-emb 8, and Ser-emb 17 in the Serpens Cluster B (Bergner et al. 2019; Martín-Doménech et al. 2019); HH-212 in the Orion Molecular Cloud Complex (Codella et al. 2016; Lee et al. 2017); and BHR-71 IRS1 in the BHR-71 Bok globule (Yang et al. 2020). In addition, a hot-corino-like atmosphere was implied toward IRAS4A1 in the Perseus 103 molecular cloud (Sahu et al. 2019). In particular, the hot corino nature of most of these corinos was found through case studies toward specific sources rather than from surveys.

In addition to the hot corino chemistry, there is also the so-called "warm-carbon-chain chemistry" (WCCC) associated with protostellar, warm (∼30 K) infalling envelopes that are abundant in unsaturated carbon-chain molecules (Sakai et al. 2008, 2009). Although the hot corino chemistry and the warm-carbon-chain chemistry exhibit two distinct behaviors, there are sources bearing signatures of both COMs and long-carbon-chain molecules. Higuchi et al. (2018) carried out a survey toward 36 Class 0/I protostars in the Perseus molecular cloud complex and showed that the abundance ratios between CH_3OH, a hot corino tracer, and ethynyl (C_2H) and cyclopropenylidene (c-C_3H_2), both being proxies for WCCC, range within a continuous spectrum of one to two orders of magnitude. While there is no distinct separation between the two types of chemical signatures, the column density ratios between ethynyl and methanol ($[C_2H]/[CH_3OH]$) appear to be correlated with the core locations in the cloud complex (Higuchi et al. 2018).

The Planck Galactic Cold Clumps (PGCC) catalog is an all-sky catalog consisting of cold clump candidates (Planck Collaboration et al. 2016). At an angular scale of ∼5′, Planck's resolution, these PGCCs appear as dense (with molecular hydrogen column density $N(H_2) > 10^{20}\,cm^{-2}$) and cold (10–20 K) regions potentially harboring star formation at their very early stages. Survey observations at 850 μm were previously conducted with the Submillimetre Common User Bolometer Array-2 (SCUBA-2) at the 15 m James Clerk Maxwell Telescope (JCMT) toward 96 dense PGCCs (clump-averaged column density larger than $5 \times 10^{20}\,cm^{-2}$) in Orion A and B and λ Orionis (Yi et al. 2018), and as part of the JCMT large program "SCOPE: SCUBA-2 Continuum Observations of Pre-protostellar Evolution" (Liu et al. 2018; Eden et al. 2019). This 850 μm (dust) continuum survey identified 119 protostellar and starless cores within 40 Orion PGCCs (Yi et al. 2018). These cores were further observed with the Nobeyama Radio Observatory (NRO) 45 m telescope to study their evolutionary stages gauged by, for example, their N_2D^+ abundances (Tatematsu et al. 2017, G. Kim et al. 2020, in preparation). On the basis of these surveys, we selected 72 dense and compact 850 μm continuum cores at early stages (starless cores with intense N_2D^+ emission and Class 0 protostellar cores with and without intense N_2D^+ emission) and carried out observations with the Atacama Compact Array (ACA) within an Atacama Large Millimeter/submillimeter Array (ALMA) project. This project, the ALMA Survey of Orion Planck Galactic Cold Clumps (ALMASOP), aims to probe the onset of star formation (see Section 2). We conducted chemical studies on the sample and report in this paper the finding of four sources that are rich in molecular lines and harbor saturated COMs. Information about the ALMA observations over the full sample will be reported in a separate paper (S. Dutta et al. 2020, in preparation).

2. Observations

The observations were carried out with the ACA, which is an interferometer composed of twelve 7 m antennas. They were conducted as a part of the ALMA Cycle 6 project (#2018.1.00302.S; PI: Tie Liu), aiming to study the fragmentation of dense cores in the Orion Molecular Cloud Complex.

The longest baseline was 49 m, which was about 37.7 $k\lambda$. The half-power beam width of the synthesized beam was ∼5.″6, and the field of view was ∼43.″2. Four spectral windows, centered at 216.6, 218.9, 231.0, and 233.0 GHz, with a uniform bandwidth of 1875 MHz (∼2500 km s^{-1}) and a resolution of ∼1.129 MHz (∼1.5 km s^{-1}) were set.

The data were calibrated with the Common Astronomy Software Applications package (CASA; McMullin 2007) version 5.4.0-68 and its pipeline version 42030M (Pipeline-CASA54-P1-B). In the pipeline, the images were processed through "tclean" with automasking and the robust parameter of the Briggs weighting set to 0.5. See the ALMA Science Pipeline website[29] for other parameters of automasking (e.g., sidelobethreshold = 1.25, noisethreshold = 5.0, and negativethreshold = 0.0).

We report the results of four sources, which we identified as hot corinos within the whole sample (see Section 4.2). They are G211.47–19.27S, G208.68–19.20N1, G210.49–19.79W, and G192.12–11.10, hereafter G211, G208, G210, and G192, respectively. See Table 1 for the coordinates, date, on-source integration time, calibrators of the observations, the sizes and position angles of beams, and the rms noise of the continuum and line images.

We note that in this paper we use only the 7 m ACA data for the hot corino identification. The ALMA 12 m array data,

[29] https://almascience.eso.org/processing/science-pipeline

Table 1
Parameters of the Observations

Source Name	α_{J2000} δ_{J2000}	Total On-source Integration Time	Beam θ_{max}, θ_{min}, PA	σ_{CONT}, σ_{Chn} mJy beam^{-1} (mK)	Date Bandpass and Flux, Phase	Calibrator
G211.47–19.27S	05:39:56.097–07:30:28.403	210 s	$8\farcs79$, $4\farcs20$, $-76\fdg5$	8.6 (5.4), 37.1 (23.3)	11/19	J0522–3627, J0607–0834
					11/27	J0854+2006, J0607–0834
G208.68–19.20N1	05:35:23.486–05:01:31.583	500 s	$7\farcs60$, $4\farcs00$, $-83\fdg3$	13.5 (10.3), 27.5 (20.9)	11/27	J0423–0120, J0542–0913
G210.49–19.79W	05:36:18.860–06:45:28.035	300 s	$7\farcs65$, $4\farcs02$, $-82\fdg4$	1.9 (1.5), 27.3 (20.5)	11/27	J0854+2006, J0607–0834
					11/27	J0522–3627, J0542–0913
					11/28	J0423–0120, J0542–0913
G192.12–11.10	05:32:19.540+12:49:40.190	480 s	$6\farcs86$, $4\farcs81$, $80\fdg7$	1.2 (0.9), 20.1 (14.1)	11/21	J0423–0120, J0530+1331
					11/26	J0423–0120, J0530+1331

Note. All of the measurements were made in 2018. The observations toward G208 and G210 were separated into five executions, and the observations toward G192 were separated into two executions. The θ_{max} and θ_{min} are the FWHM of the synthesized beam along the major and minor axes, respectively, PA is the beam position angle, and σ_{CONT} and σ_{Chn} are the rms noises of the measurement spanning over 7.5 GHz (continuum) and 1.129 MHz (spectral resolution), respectively. The brightness temperatures of σ_{CONT} and σ_{Chn} are derived with 230 GHz and the synthesized beam area of each source (see Table 2).

which provide better angular resolutions, will be employed for further analyses, such as the structures of the line-emitting regions, in a forthcoming paper.

3. Results

3.1. Dust Continuum

The continuum images of the four sources are shown in Figure 1. All four sources are well detected with a single dominant component in the map centers, and their peak brightness temperatures are all less than 1 K. Such brightness temperatures are much less than the expected physical temperature (greater than 10 K in protostars), so their continuum emission is optically thin. The images for the two brighter targets (G211 and G208) are severely dynamical-range limited (i.e., the residual sidelobe features dominate over the ideal theoretical noise, 5×–10× in our cases) and hence noisier than maps for the other two targets, as indicated in Table 1. In addition to the compact component, an extended component in G210 exists, and it is possibly the remnant of the envelope. We applied a 2D Gaussian fit in CASA to the continuum. Based on the fitting result, including the source-averaged flux, the peak positions, the integrated flux density, and the apparent and deconvolved angular sizes, we calculated the molecular hydrogen column density ($N_{\rm H_2}$), the mass (M), and the radius (R) of the sources with formulae modified from Equations (A.26) and (A.30) in Kauffmann et al. (2008) for optically thin continuum emission.

The source-averaged molecular hydrogen column density $N_{\rm H_2}$ can be derived via

$$N_{\rm H_2} = \frac{F_{\rm CONT}^{\rm Int}}{\Omega_S\, \mu_{\rm H_2}\, m_{\rm H}\, \kappa_\nu\, B_\nu(T_{\rm d})} \quad (1)$$

where $F_{\rm CONT}^{\rm Int}$ is the total flux, Ω_S is the size of the deconvolved source image, $\mu_{\rm H_2}$ is the molecular weight per hydrogen molecule ∼2.8, $m_{\rm H}$ is the mass of the hydrogen atom, $B_\nu(T_{\rm d})$ is the blackbody radiation function evaluated at the dust temperature $T_{\rm d}$, and κ_ν is the dust opacity in the form of $\kappa_\nu = 0.1(\nu/1\ {\rm THz})^\beta\ {\rm cm^2\ g^{-1}}$ where β is the the dust opacity index (Beckwith et al. 1990). The indices β were assumed to be 1.70, which is the typical opacity index of cold clumps in the submillimeter band (Juvela et al. 2018), and the resulting κ_ν at 1.3 mm is 0.0083 $\rm cm^2\ g^{-1}$. Since the continuum emission of all four sources is marginally resolved (i.e., the observed source size is larger than but comparable to the synthesized beam size), the derived column densities could be lower limits.

The mass is estimated via

$$M = \frac{F_\nu\, D^2}{\kappa_\nu\, B_\nu(T_{\rm d})} \quad (2)$$

where D is the distance to the source adopted from the PGCC catalog (Planck Collaboration et al. 2016). The sources are marginally resolved, and the radii of the sources were estimated via

$$R = \frac{1}{2}\, D\, \theta_S \quad (3)$$

where θ_S is the deconvolved FWHM size of the source derived from the 2D fit to the continuum data. All of the derived quantities are presented in Table 2. We note that the gas column density and mass are estimated with a range of dust temperatures at 50, 100, and 150 K.

According to the coordinates of the continuum peaks, we searched for known young stellar objects (YSOs) within 5″ using SIMBAD[30] (Wenger et al. 2000). We found that three of the four sources are likely to be associated with the Herschel Orion Protostar Survey (HOPS) objects (Manoj et al. 2013), HOPS 288 for G211, HOPS 87 for G208, and HOPS 168 for G210, which are all located in the Orion A molecular cloud (see Table 3). First, the offsets between each source and its corresponding HOPS object are small (0.″7, 2.″17, and 0.″84 for G211, G208, and G210, respectively). Second, there are no other compact sources within each of their fields of view. In contrast, G192 in λ Orionis is first identified as a YSO. See Section 4.1 for more discussions.

3.2. Molecular Emission

We extracted the spectra at the continuum peak in the four spectral data cubes for each of the 72 sources in the project (see Section 1). We then scanned all of the samples and identified only those containing rich spectral features including particularly multiple CH_3OH lines with excitation temperature higher than 100 K for further analysis. With the above criteria, we identified four sources (G211, G208, G210, and G192) and present their spectra, respectively, in Figures A1–A4. In total, around 154 molecular lines in G211, 80 lines in G208, 38 lines in G210, and 30 lines in G192 above $3\sigma_{\rm Chn}$ were recognized. We further applied Gaussian fitting over those transitions to obtain the observed frequency ($f^{\rm obs}$), peak brightness temperature ($T_{\rm p}$), velocity width (Δv), and integrated intensity (w) of the identified lines. The results of the Gaussian fitting to each line of each source are in Tables B1, B2, B3, and B4 for G211, G208, G210, and G192, respectively.

For line identifications, we searched the Splatalogue,[31] which is an online database including the Jet Propulsion Laboratory Molecular Spectroscopy (JPL,[32] Pickett et al. 1998) and the Cologne Database for Molecular Spectroscopy (CDMS,[33] Müller et al. 2005) catalog for astronomical spectroscopy, for possible molecule candidates. We detected 25 molecular species (including isotopologues) in G211, 18 in G208, 18 in G210, and 16 in G192. Some species were detected in all four sources, including CO, $C^{18}O$, OCS, ^{13}CS, H_2S, HCCCN, DCN, DCO^+, D_2CO, H_2CO, c-C_3H_2, CCD, ^{34}SO, HCOOH, and CH_3OH. Two molecules were detected in three of the four sources: HNCO (not in G208) and SiO (not in G192). CH_3CHO and $HCOOCH_3$ were detected in G211 and G208 but were not found in the other two sources. SO_2 is detected in G211 and G208. Among the four sources, G211 is the most line-rich target, in which C_2H_5OH, NH_2CHO, and isotopologue species including $^{13}CH_3OH$, CH_2DOH, $^{13}CH_3CN$, and $HC^{13}CCN$ were identified. G210 and G192 seem to have similar molecular composition. We consolidate and present in Table C1 the molecular line parameters, such as their rest frequencies, quantum numbers, and excitation energies, for the identified species and transitions.

Spectra of the molecule candidates were then modeled with the eXtended CASA Line Analysis Software Suite (XCLASS,[34] Möller et al. 2017), which is a CASA toolbox

[30] http://simbad.u-strasbg.fr/simbad/
[31] https://www.cv.nrao.edu/php/splat/
[32] https://spec.jpl.nasa.gov/
[33] https://cdms.astro.uni-koeln.de/
[34] https://xclass.astro.uni-koeln.de/

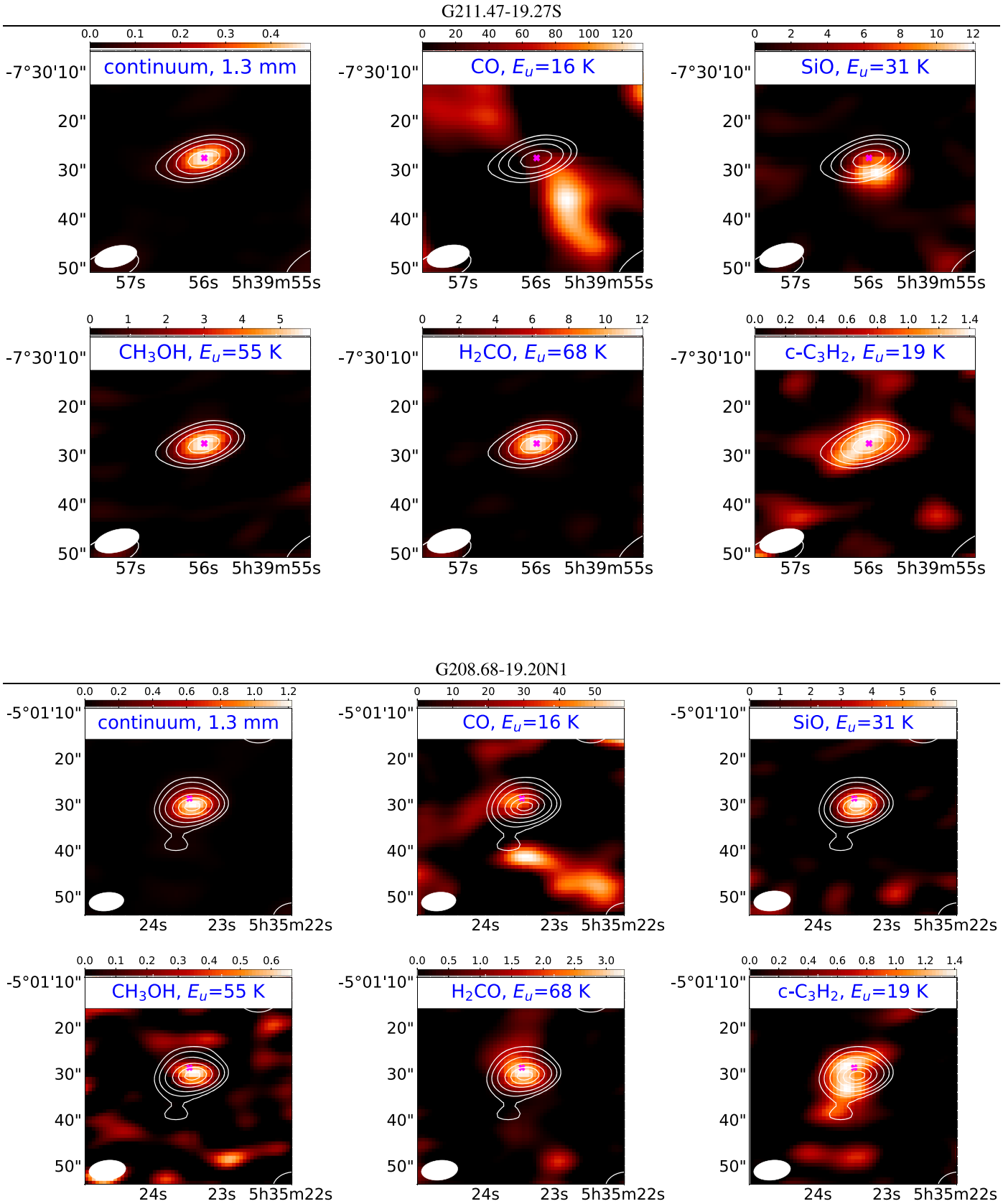

Figure 1. Moment 0 images of (from left to right, from top to bottom) continuum, CO (2–1, $f_{\rm rest}$ = 230,538 MHz, E_u = 16 K), SiO (5–4, $f_{\rm rest}$ = 217,105 MHz, E_u = 31 K), CH_3OH (5(1,4)–4(2,3) E, $f_{\rm rest}$ = 216,946 MHz, E_u = 55 K), H_2CO (3(2,2)–2(2,1), $f_{\rm rest}$ = 218,476 MHz, E_u = 68 K), and c-C_3H_2 (3(3,0)–2(2,1), $f_{\rm rest}$ = 216,279 MHz, E_u = 68 K). The contours represent the continuum at [5, 10, 20, 40, 60, 80]$\sigma_{\rm CONT}$ where $\sigma_{\rm CONT}$ is the rms noise of each continuum (see Table 2). The color scale of the continuum and the other moment 0 images is in units of Jy beam^{-1} and Jy beam^{-1} km s^{-1}. The magenta marker is the location of each corresponding Herschel Orion Protostar Survey object (see Table 3). Note that there is no SiO J = 5–4 transition detection in G192.12–11.10.

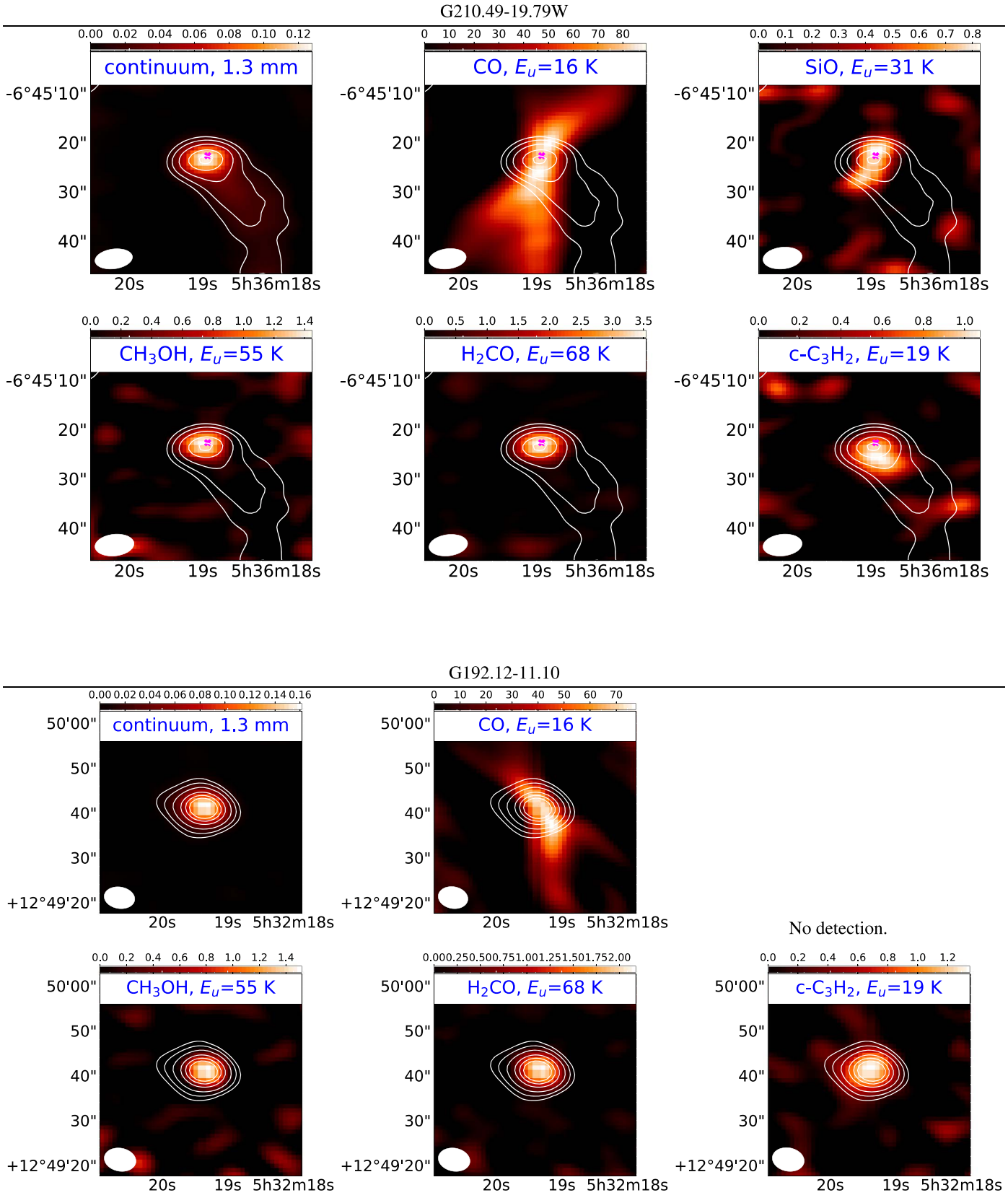

Figure 1. (Continued.)

for molecular line synthesis. In myXCLASS, a function of XCLASS, each (gaseous) component of a molecule is assumed to be in its individual local thermodynamic equilibrium (LTE). This means that the source function is in the form of a Planck function with a rotational temperature ($T_{\rm rot}$) that is expected to be the same as its kinetic temperature if all of the levels are thermalized (Goldsmith & Langer 1999; Möller et al. 2017). To execute myXCLASS, users need to define the

Table 2
Parameters and Results of the Continuum Analysis

Source Name	θ_A ($''$)	θ_S ($''$)	$F_{\rm CONT}^{\rm Int}$ (mJy)	D (pc)	$N_{\rm H_2}$ ($\rm cm^{-2}$) 50 K	100 K	150 K	M ($M_\odot$) 50 K	100 K	150 K	R (au)
G211.47–19.27S	6.07	2.22	552	415	1.63e+24	7.73e+23	5.06e+23	0.82	0.39	0.25	461
G208.68–19.20N1	5.51	2.51	1530	415	3.55e+24	1.68e+24	1.10e+24	2.28	1.08	0.71	520
G210.49–19.79W	5.55	3.42	185	415	2.31e+23	1.09e+23	7.16e+22	0.28	0.13	0.09	709
G192.12–11.10	5.74	2.87	199	400	3.52e+23	1.66e+23	1.09e+23	0.28	0.13	0.09	575

Note. The θ_A is the FWHM of the synthesized beam; θ_S is the FWHM of the deconvolved source image; θ_A and θ_S are the geometric mean of their maximum and minimum FWHM values, that is, $\theta = \sqrt{\theta_{\rm max}\theta_{\rm min}}$; $F_{\rm CONT}^{\rm Int}$ is the total flux integrated over the source; $N_{\rm H_2}$, M, and R are the calculated column density of molecular hydrogen, the mass, and the radius of the sources, respectively. The $N_{\rm H_2}$ and M are estimated at three different dust temperatures, 50, 100, and 150 K. Note that column densities listed here could be lower limits. See Section 3.1.

rotational temperature ($T_{\rm rot}$), the size (θ_C), the column density (N), the local-standard-of-rest velocity ($v_{\rm LSR}$), and the velocity width (Δv) of each component. These parameters are assumed to be identical for all transitions of each molecular component. By solving the radiative transfer equation for an isothermal object in one dimension with the given molecular component parameters, myXCLASS generates the synthetic spectrum and provides the transition list, intensity profiles, and optical depth profiles of each component. We further employed Modeling and Analysis Generic Interface for eXternal numerical codes (MAGIX; Möller et al. 2013), another CASA package, to optimize these molecular component parameters within the given ranges through the XCLASS interface. XCLASS also provides the transition information based on the CDMS and JPL databases.

In our study, we fixed the component sizes (θ_C) to be the same as the deconvolved dust continuum (i.e., $\theta_C = \theta_S$) except for carbon monoxide $C^{18}O$, and we optimized the other parameters using MAGIX. We note that this size may be overestimated for molecules (e.g., COMs) with compact emission and lead to underestimation of their column densities. For the extended molecules (e.g., carbon-chain molecules), this size may be underestimated, but the column density averaged within the beam should be correctly estimated. Some molecules (e.g., hydrogen sulfide H_2S and sulfur monoxide ^{34}SO) that are commonly detected in star-forming regions were detected with only one line, so their (rotation) temperature could not be estimated, and they were fixed to be 100 K for their molecular column density calculation. We executed MAGIX for each molecule individually to find their corresponding best fit. With those numbers as inputs, we then executed a final run including all species for global optimization. Table 4 shows the results from MAGIX optimization for G211, G208, G210, and G192. The parameter uncertainties estimated by the error estimation function of MAGIX are also presented. We also mark in Table 4 the molecules that are unresolved in their moment 0 map. The hydrocarbons and the carbon-chain molecules are resolved while saturated COMs are not, indicating that they are tracing the cold and the warm/hot regions, respectively. The sulfur-bearing molecules are in general unresolved as well, and they might be tracing the central region of the outflows due to their large line widths. See Section 4 for more discussions.

A population diagram (or rotational diagram) is a common tool for estimating the rotational temperature and the column density (Goldsmith & Langer 1999). Figure D1 shows the population diagram of CH_3OH in each source, and the derived column densities and rotational temperatures are all consistent with the estimation of MAGIX. See Appendix D for the details.

4. Discussion

4.1. Source Overview

All four sources, except for G192, have been identified as YSOs in previous studies. G211, G208, and G210 were first identified as YSOs (MGM2012 518, 2433, and 777, respectively) in a mid-IR (spanning 3–24 μm) survey toward the Orion A and B clouds conducted with the Spitzer Space Telescope (Megeath et al. 2012). G211 and G210 were also identified as YSOs (FKV2013 771 and 593, respectively) in a survey from 0.4 to 24 μm toward the LYNDS 1641 cloud, which is a star-forming region in Orion A (Fang et al. 2013). G208, on the other hand, also coincides with OMC3/MMS6 (Chini et al. 1997). These three sources were further classified as Class 0 protostars (Furlan et al. 2016).

The three sources are also subjects of outflow studies in the literature (e.g., Fischer et al. 2010; Velusamy et al. 2014; Manoj et al. 2016; Watson et al. 2016; van Kempen et al. 2016). From our observations, the carbon monoxide CO $J = 2$–1 images show a clear biconical outflow morphology in G211 and G210 (see Figure 1). In addition, silicon monoxide SiO is known as a good probe of shocks. The spatial distribution of the SiO $J = 5$–4 emission in G211 and G210 is consistent with their outflows (see Figure 1). Although no obvious outflow signature appears in our G208 CO $J = 2$–1 image, Takahashi & Ho (2012) and Takahashi et al. (2019) have detected a very compact 5–4 ($<5''$) bipolar molecular outflow in the CO $J = 3$–2 and 2–1 lines, respectively, indicating the object is in an extremely young stage of formation. Our detection of compact SiO emission is consistent with what was inferred by Takahashi & Ho (2012).

G192 is the only object in λ Orionis among the four sources. While it has not been associated with any known YSOs in the literature, our observations indicate the presence of biconical outflow in its CO $J = 2$–1 emission.

4.2. Hot Corino Identification

A hot corino is normally identified according to its compact (<100 au), abundant, and presumably passively thermally evaporated COMs (Herbst & van Dishoeck 2009). Methanol (CH_3OH), as the root of the COMs in the grain origin scheme in particular, is considered to be an important indicator of the presence of hot corinos. Toward all four sources (G211, G210,

Table 3
Coordinates of the Continuum Peaks and Information on Their Corresponding HOPS Objects and Protostellar Classifications

Source Name	Cloud	$\alpha^{\rm peak}_{\rm J2000}$	$\delta^{\rm peak}_{\rm J2000}$	HOPS (Furlan et al. 2016)					
				Index	$\alpha_{\rm J2000}$	$\delta_{\rm J2000}$	Class	$L_{\rm bol}$ ($L_\odot$)	$T_{\rm bol}$ (K)
G211.47–19.27S	Orion A	05:39:55.988	−07:30:27.593	HOPS 288	05:39:55.95	−07:30:28.0	0	135.47	48.6
G208.68–19.20N1	Orion A	05:35:23.434	−05:01:30.803	HOPS 87	05:35:23.47	−05:01:28.7	0	36.49	38.1
G210.49–19.79W	Orion A	05:36:18.965	−06:45:23.355	HOPS 168	05:36:18.93	−06:45:22.7	0	48.07	54.0
G192.12–11.10	λ Orionis	05:32:19.345	+12:49:41.140	…	…	…	…	…	…

G192, and G208), we detected CH_3OH with a very compact distribution (see Figure 1). Similar to the continuum analysis, we tried to used CASA 2D Gaussian fitting to fit the CH_3OH integrated intensity maps. The distributions of CH_3OH emission, even for the transition with the low excitation energy (E_u ∼55 K) we have, are very compact as the fitting routine suggested the sources to be unresolved. Additionally, the high rotational temperatures (>165 K) are also consistent with and indicative of thermal evaporation of icy CH_3OH. Unlike the often extended CH_3OH emission seen in cold, dark clouds (Friberg et al. 1988), cold, massive prestellar clumps (Sanhueza et al. 2013), or outflow (Araya et al. 2008), the evidence we present suggests the four objects are hot corinos. Further studies with higher angular and spectral resolutions would help to solidify (or falsify) this classification.

Both COMs and carbon-chain molecules are detected in our four sources. Lefloch et al. (2018) proposed a classification scheme based on the ratio of the number of oxygen-bearing molecular species over that of the hydrocarbon species. While the scheme was not related to any chemical models but was rather phenomenological, the oxygen-bearing and hydrocarbon molecules are of the type $C_xH_yO_z$ and C_zH_y, respectively. In our samples, the values of their ratio are all larger than 1.9, which is the lower limit suggested by Lefloch et al. (2018) for a hot corino. Note that in this classification the nitrogen- and sulfur-bearing molecules are not involved in the definitions.

Table 5 shows the fractional column density, X, of COMs relative to hydrogen. The fractional column densities of methanol $X(CH_3OH)$ are larger than 10^{-8}, which is typical of a hot corino, except in G208. In addition to methanol, there are more COMs (e.g., acetaldehyde CH_3CHO and methyl formate $HCOOCH_3$) detected in G211 and G208. In G208, $X(CH_3CHO)$ and $X(HCOOCH_3)$ are 4.1×10^{-10} and 6.6×10^{-10}, respectively, and they are 5 and 20 times larger, respectively, in G211. Ethanol C_2H_5OH is also detected in G211, and $X(C_2H_5OH)$ is 2.69×10^{-8}, comparable to the value in IRAS 16293–2422 B (Jørgensen et al. 2018, see Table 5). The brightness temperatures of all these COM emissions are well below <1 K, implying these emissions are optically thin. However, if some of these lines suffer severely from beam dilution, their opacities could be higher, which will lead to higher fractional column densities.

Table 6 shows the fractional column densities of COMs with respect to CH_3OH ([COM]/[CH_3OH]). In IRAS 16293–2422 B, B335, and HH-212, [CH_3CHO]/[CH_3OH] is roughly half of [$HCOOCH_3$]/[CH_3OH] and [C_2H_5OH]/[CH_3OH]. In our sources, CH_3CHO and $HCOOCH_3$ are detected in G211 and G208, and C_2H_5OH is detected in G211. The ratio [CH_3CHO]/[CH_3OH] in G211 is comparable to that in B335 and HH-212; however, [CH_3CHO]/[CH_3OH], [$HCOOCH_3$]/[CH_3OH], and [C_2H_5OH]/[CH_3OH] in G211 and G208 (without C_2H_5OH) are an order of magnitude larger than the typical values in other hot corinos.

The discrepancy in these ratios could result from a few possibilities. First, it may be due to different beam-dilution factors of different COM emissions. In the current analyses, we have assumed that all COM emissions originate from the same extent as the dust continuum. As noted earlier, the COM emissions in fact appear to be more compact than the continuum emission. The COM emission size may have been overestimated, leading to underestimations of the COM column densities. We speculate a more compact CH_3OH emission size (than the continuum as well as $HCOOCH_3$ and C_2H_5OH), which may correspond to a higher CH_3OH column density and hence reduces [$HCOOCH_3$]/[CH_3OH] and [C_2H_5OH]/[CH_3OH]. Our current spatial resolution is not yet sufficient to fully resolve the region from where the COM emission is emitted. Future investigations using the 12 m ALMA data may help to validate this scenario.

Second, CH_3OH abundances in our sources may have been underestimated because of opacity. A hint of this is the column density ratio of methanol and its isotopologues. In G211, the ratio of methanol isotopologues $^{12}C/^{13}C$ derived from [CH_3OH]/[$^{13}CH_3OH$] is ∼10, which is lower than the typical $^{12}C/^{13}C \sim 70$ in the local interstellar medium (ISM; Wirström et al. 2011). The ratio appears comparable to [CH_3OH]/[$^{13}CH_3OH$] of other Class 0 hot corinos, for example, 24 in HH-212 (Lee et al. 2019, see Table 7). CH_3OH transitions with high optical depths have been observed in Taquet et al. (2015) and Lee et al. (2019) for the cases of IRAS 2A and HH-212, respectively. If we assume that the CH_3OH column density in G211 is seven times larger in order to make $^{12}C/^{13}C$ compatible with the local ISM, the high [COM]/[CH_3OH] observed in our sources will be reduced. In this case, however, the deuteration ratios of CH_3OH ([CH_2DOH]/[CH_3OH], Table 7) and [CH_3CHO]/[CH_3OH] become small compared to the others. Instead, we can estimate those [COM]/[CH_3OH] ratios in G211 by utilizing the column density of $^{13}CH_3OH$ as a proxy for CH_3OH, assuming the $^{13}CH_3OH$ emission is optically thin and a $^{12}C/^{13}C$ of 70. As shown in Table 6, the [COM]/[CH_3OH] ratios in G211 appear comparable to the other hot corino sources.

Finally, Bergner et al. (2019) compared the [COM]/[CH_3OH] ratio in hot corinos Ser-emb 1, Ser-emb 8, and Ser-emb 17 with other hot corinos and found that it spanned two orders of magnitude. They suggested this variation is the result of the local environment or the time-dependent warm-up chemistry.

The only COM detected in G210 and G192 is CH_3OH. Assuming other COMs such as CH_3CHO and $HCOOCH_3$ bear similar [COM]/[CH_3OH], their column densities would be

Table 4
Molecule Component List Calculated by MAGIX

Formula	G211.47–19.27S				G208.68–19.20N1				G210.49–19.79W				G192.12–11.10			
	T_{rot} (K)	N (cm^{-2})	v_{LSR} (km s^{-1})	Δv (km s^{-1})	T_{rot} (K)	N (cm^{-2})	v_{LSR} (km s^{-1})	Δv (km s^{-1})	T_{rot} (K)	N (cm^{-2})	v_{LSR} (km s^{-1})	Δv (km s^{-1})	T_{rot} (K)	N (cm^{-2})	v_{LSR} (km s^{-1})	Δv (km s^{-1})
CH_3OH	185 ± 4	8.5E+16 (0.1)†	2.2	6.2	298 ± 3	4.9E+15 (0.1)†	10.4	4.1	155 ± 3	7.1E+15(0.1)†	8.1	9.8	173 ± 5	7.2E+15 (0.2)†	9.6	9.2
$^{13}CH_3OH$	156 ± 6	9.2E+15 (0.1)†	2.0	7.7	…	…	…	…	…	…	…	…	…	…	…	…
CH_2DOH	67 ± 5	2.3E+16 (0.1)†	1.8	6.0	…	…	…	…	…	…	…	…	…	…	…	…
CH_3CHO	127 ± 4	1.4E+15 (0.1)†	2.4	4.9	223 ± 5	5.6E+14 (0.1)†	11.0	2.8	…	…	…	…	…	…	…	…
CH_3OCHO	197 ± 6	8.5E+15 (0.1)†	3.3	7.8	143 ± 3	1.2E+15 (0.1)†	11.4	1.7	…	…	…	…	…	…	…	…
C_2H_5OH	304 ± 6	1.7E+16 (0.1)†	1.5	7.2	…	…	…	…	…	…	…	…	…	…	…	…
$^{13}CH_3CN$	295 ± 6	8.2E+13 (0.1)†	2.4	7.0	…	…	…	…	…	…	…	…	…	…	…	…
CCD	62 ± 6	2.3E+14 (0.1)	4.8	2.2	24 ± 3	8.1E+13 (0.1)	11.1	1.4	24 ± 3	4.3E+13 (0.1)	8.7	2.0	19 ± 4	5.5E+13 (0.2)	10.3	2.3
c-C_3H_2	32 ± 4	1.2E+14 (0.1)	5.1	3.1	22 ± 3	5.7E+13 (0.1)	11.0	1.0	20 ± 3	2.2E+13 (0.1)	8.6	1.7	13 ± 5	3.7E+13 (0.2)	10.4	1.8
H_2CO	189 ± 4	8.2E+15 (0.1)	4.6	4.9	39 ± 3	5.9E+14 (0.1)	11.1	1.6	51 ± 3	2.7E+14 (0.1)	8.4	2.6	45 ± 5	2.9E+14 (0.2)	10.5	2.8
D_2CO	136 ± 5	3.5E+14(0.1)†	3.9	4.6	38 ± 3	5.7E+13 (0.1)	11.2	1.9	40 ± 3	2.4E+13 (0.1)	8.4	2.2	22 ± 5	3.3E+13 (0.2)	10.5	2.3
DCO^+	100	2.6E+13 (0.2)	4.8	2.4	100	2.9E+13 (0.1)	11.3	1.8	100	9.1E+12 (0.1)	8.3	1.3	100	1.8E+13 (0.2)	10.4	2.0
N_2D^+	…	…	…	…	100	1.9E+12 (0.1)	11.9	1.4	…	…	…	…	…	…	…	…
HCOOH	100	9.2E+14 (0.1)†	1.5	4.3	100	3.5E+13 (0.1)†	10.8	0.8	100	7.7E+13 (0.1)†	8.1	6.5	100	1.2E+14 (0.2)†	9.9	7.2
DCN	100	4.0E+13 (0.1)	4.3	4.8	100	1.2E+13 (0.1)	11.1	1.7	100	7.3E+12 (0.1)	8.5	3.1	100	6.8E+12 (0.2)	10.5	3.2
HCCCN	100	5.0E+13 (0.1)	4.3	5.3	100	1.3E+13 (0.1)†	11.3	3.4	100	7.1E+12 (0.1)†	8.2	4.9	100	6.0E+12 (0.2)†	11.0	5.3
$HC^{13}CCN$	100	1.6E+13 (0.2)†	5.0	5.9	…	…	…	…	…	…	…	…	…	…	…	…
HNCO	205 ± 4		2.5	7.8	…	…	…	…	161 ± 4		8.4	10.0	100		10.8	5.5

Table 4
(Continued)

Formula	G211.47–19.27S				G208.68–19.20N1				G210.49–19.79W				G192.12–11.10			
	T_{rot} (K)	N (cm^{-2})	v_{LSR} (km s^{-1})	Δv (km s^{-1})	T_{rot} (K)	N (cm^{-2})	v_{LSR} (km s^{-1})	Δv (km s^{-1})	T_{rot} (K)	N (cm^{-2})	v_{LSR} (km s^{-1})	Δv (km s^{-1})	T_{rot} (K)	N (cm^{-2})	v_{LSR} (km s^{-1})	Δv (km s^{-1})
		1.2E+15 (0.1)†								1.2E+14 (0.1)†				3.8E+13 (0.2)†		
NH_2CHO	295 ± 6	3.6E+14 (0.1)†	2.5	7.7	…	…	…	…	…	…	…	…	…	…	…	…
H_2S	100	2.1E+15 (0.1)†	3.2	5.8	100	1.6E+15 (0.1)†	11.2	1.9	100	1.7E+14(0.1)†	9.2	3.8	100	3.5E+14 (0.2)†	10.6	6.7
^{13}CS	100	5.5E+13 (0.1)†	4.3	5.3	100	3.2E+13 (0.1)	11.1	1.8	100	3.6E+12 (0.1)†	8.4	2.1	100	6.3E+12 (0.2)†	10.4	3.4
OCS	70 ± 4	2.1E+15 (0.1)†	3.0	5.8	122 ± 3	4.3E+14 (0.1)†	11.5	2.1	127 ± 6	2.3E+14 (0.1)†	8.5	7.3	86 ± 5	2.4E+14 (0.2)†	10.5	7.7
^{34}SO	100	2.1E+14 (0.1)†	4.8	6.9	100	6.8E+13 (0.1)	11.2	2.8	100	3.8E+13 (0.1)†	11.5	13.9	100	2.8E+13 (0.2)†	10.6	3.1
SO_2	100	3.0E+15 (0.2)†	4.1	12.7	…	…	…	…	100	6.2E+14 (0.1)†	10.2	9.6	…	…	…	…
SiO	100	5.9E+13 (0.1)†	8.9	13.1	100	4.3E+13 (0.1)†	30.2	40.5	100	3.3E+12 (0.1)†	8.9	5.1	…	…	…	…
					100	2.9E+13 (0.1)†	−16.1	16.7								
$C^{18}O$	100	1.3E+16 (0.1)	5.0	3.2	100	2.0E+16 (0.1)	11.2	1.5	100	1.4E+16 (0.1)	8.3	1.7	100	1.9E+16 (0.2)	10.5	2.4

Note. The T_{rot} is the rotational temperature, and $T_{rot} = 100$ K without any error interval is fixed in the MAGIX simulation. The N is the column density, and the value in brackets is the standard deviation in $\log_{10} N$. Their values 0.1–0.2 correspond to fractional errors ranging around 25%–70%. The v_{LSR} is the local standard of rest velocity, and the Δv is the velocity width. Their standard deviation values are around 0.4 km s^{-1}. The component size of $C^{18}O$ is assumed to be 8″. The SiO profile in G208 was assumed to be constituted of two components. The daggers mark the unresolved molecules (i.e., observed source sizes are smaller than the synthesized beam size on the moment 0 map); note that the column densities of these spatially unresolved molecules may be underestimated.

Table 5
Fractional Column Density with Respect to H_2 of the COMs in Hot Corinos

$\times10^{-9}$	CH_3OH	CH_3CHO	$HCOOCH_3$	HNCO	HCOOH	NH_2CHO	C_2H_5OH	Reference
G211.47–19.27S	110	2.09	13.1	1.64	1.32	0.51	26.9	
G208.68–19.20N1	2.92	0.41	0.66	⋯	0.03	⋯	⋯	
G210.49–19.79W	64.9	⋯	⋯	1.16	0.76	⋯	⋯	
G192.12–11.10	43.5	⋯	⋯	0.26	0.83	⋯	⋯	
IRAS 16293–2422 B	833	10.0	21.7	⋯	4.67	⋯	19.2	(1), (2)
B335	380	2.40	4.60	17.0	4.70	0.40	3.80	(3)
HH-212	160	3.90	8.40	⋯	5.3	0.42	7.10	(4)

Note. This fractional column density of CH_3OH may be affected by its opacity (see Section 4.2).
References. (1) Jørgensen et al. (2018), (2) Jørgensen et al. (2016) (3) Imai et al. (2016), (4) Lee et al. (2019).

Table 6
Fractional Column Density of COMs Relative to CH3OH, [COM]/[CH_3OH]

$\times10^{-3}$	CH_3CHO	$HCOOCH_3$	C_2H_5OH	Reference
G211.47–19.27S	18.9	119	243	
G211.47–19.27S[a]	2.0	12.9	26.4	
G208.68–19.20N1	141	225	⋯	
IRAS 16293–2422 B	12.0	26.0	23.0	(1)
B335	6.32	12.1	10.0	(2)
HH-212	24.4	52.5	44.4	(3)

Note.
[a] The column density of CH_3OH is derived from the column density of $^{13}CH_3OH$ assuming the $^{12}C/^{13}C$ ratio is 70.
References. (1) Jørgensen et al. (2018), (2) Imai et al. (2016), (3) Lee et al. (2019).

Table 7
Column Density Ratios between Isotopes of Formaldehyde and Methanol in Other Hot Corinos

	$\frac{[D_2CO]}{[H_2CO]}$	$\frac{[CH_2DOH]}{[CH_3OH]}$	$\frac{[CH_3OH]}{[^{13}CH_3OH]}$	Reference
G211.47–19.27S	0.043	0.27	9.2	
IRAS 16293–2422 B	0.006	0.37	⋯	1
HH-212	⋯	0.12	24	2
IRAS 4B	0.046	0.43	⋯	3
IRAS 2A	0.052	0.62	26	3, 4

References. (1) López-Sepulcre et al. (2017) (2) Lee et al. (2019) (3) Parise et al. (2006) (4) Taquet et al. (2015).

below $\sim10^{14}$ cm^{-2} and become hardly detected, as is the case here.

4.3. Formaldehyde (H_2CO)

Once CO is frozen onto grain surfaces, formaldehyde (H_2CO) can be formed via hydrogen addition reactions from CO and then further forms CH_3OH, and their photodissociated radicals are parents of some COMs synthesized via both ice and gas-phase chemistry (Herbst & van Dishoeck 2009). H_2CO and CH_3OH are detected in all four of our sources, and they seem to show similarly compact distributions (see Figure 1). Although H_2CO and CH_3OH are detected in similar regions, the excitation temperatures of the two species are different in G208, G210, and G192. Assuming that their kinetic temperatures are the same, it indicates that their energy levels may not be thermalized.

H_2CO and its isotopologue, double-deuterated formaldehyde (D_2CO), are both detected in all of our hot corino sources. Their rotational temperatures are intermediate among the species detected with more than one transition and hence with temperatures estimated from XCLASS, and their line widths are intermediate as well.

4.4. Formamide (NH_2CHO)

Studies show that formamide NH_2CHO is a potential key species in prebiotic evolution. It has been proposed as one of the main components of both (pre)genetic and (pre)metabolic processes (Saladino et al. 2012). In G211, the fractional abundances with respect to H_2 of formamide ($X(NH_2CHO)$) and of isocyanic acid (X(HNCO)) are 1.3×10^{-10} and 4.1×10^{-10}, respectively. They are within the ranges (from 10^{-11} to 10^{-9} and from 10^{-12} to 10^{-8}, respectively) in star-forming regions with H_2CO detections (López-Sepulcre et al. 2015).

The [NH_2CHO])/[HNCO] in G211 is about 0.32, which is comparable to 0.14 in the hot corino L483 (Oya et al. 2017). Furthermore, it was suggested that NH_2CHO is chemically related to HNCO, and their abundances follow a tight correlation, $X(NH_2CHO) = 0.04\,X(HNCO)^{0.93}$, in star-forming regions with H_2CO detection (López-Sepulcre et al. 2015). $X(NH_2CHO)$ in G211 is 5.1×10^{-10}, which is comparable to the value estimated by the above formula (2.7×10^{-10}). The formation mechanism of NH_2CHO supported by this tight correlation is the hydrogenation of HNCO in icy grain mantles (Raunier et al. 2004; Garrod et al. 2008; Jones et al. 2011; López-Sepulcre et al. 2015). However, a recent laboratory experiment suggested that this pathway of NH_2CHO forming from the hydrogenation of HNCO is insufficient (Noble et al. 2015).

Another mechanism of NH_2CHO formation is via the reactions between NH_4^+ and H_2CO in the gas phase: (1) the radiative association reaction and the subsequent dissociative recombination of NH_2CHO^+ (Quan & Herbst 2007), (2) the ion–molecule reaction and the subsequent electron recombination of NH_3CHO^+ (Halfen et al. 2011), and (3) the reaction between amidogen and formaldehyde (NH_2+H_2CO, Barone et al. 2015). In HH-212, the NH_2CHO and the D_2CO have similar spatial distributions. This indicates the possible correlation between NH_2CHO and H_2CO and further supports the formation of NH_2CHO from H_2CO in the gas phase (Lee et al. 2017). Due to the limitation of the spatial resolution, we are not able to examine the spatial correlation between them.

Finally, a laboratory experiment showed that NH_2CHO is also possibly formed via icy mixtures of carbon monoxide and ammonia (i.e., CO:NH_3) irradiated by energetic particles such as electrons (Jones et al. 2011). Moreover, the UV

photoprocessing of CO:NH_3 and CO:CH_4 ice samples produces NH_2CHO and CH_3CHO, respectively, and the predicted abundance of NH_2CHO is 2–16 times larger than that of CH_3CHO (Martin-Domenech et al. 2020). This is opposite to the current observations via the other hot corinos as well as our studies (e.g., ∼0.1 in HH-212, Lee et al. 2019), so an additional chemical mechanism may be required.

In G210 and G192, X(HNCO) values are 1.2×10^{-9} and 2.6×10^{-10}, respectively, which are within the range presented by López-Sepulcre et al. (2015). Their $X(NH_2CHO)$ values are estimated to be $\sim 10^{-10}$, and their column densities of NH_2CHO are therefore estimated to be on the order of $\sim 10^{13}$, which may be insufficient to be detected.

4.5. Hydrocarbons and Long-carbon-chain Molecules

Deuterated ethynyl (CCD), cyclopropenylidene (c-C_3H_2), and cyanoacetylene (HCCCN and $HC^{13}CCN$ in G211), which bear carbon chains or carbon rings, are also detected. The estimated rotational temperatures of CCD and c-C_3H_2 are distinctly cooler (∼25 K and ∼15 K, respectively) in G208, G210, and G192, and slightly warmer (∼63 K and ∼32 K, respectively) in G211. This is consistent with the trend that temperatures are warmer in G211 for all of the species. The cooler temperatures of these species are also compatible with their more extended emission presented in Figure 1. Meanwhile, their line widths are narrow ($\Delta v < 2.5$ km s^{-1} in 208, G210, and G192 and $\Delta v < 3.5$ km s^{-1} in G211) compared with the line widths of the COMs and the outflow tracers.

HCCCN, a long-carbon-chain molecule, is detected in all four sources, but its line widths are wider than that of CCD and c-C_3H_2. Assuming the rotational temperature of HCCCN is 100 K, the column density of HCCCN is in general higher than that of c-C_3H_2 and CCD within an order of magnitude.

$HC^{13}CCN$, which is an isotopologue of HCCCN, is detected in G211 only. Under the assumption of $T_{\rm rot} = 100$ K, the ratio [$HC^{13}CCN$]/[HCCCN] ∼ 0.33. While here we assumed an excitation temperature higher than the calculated value of the other carbon-chain molecule (i.e., CCD), the derived isotopic ratio is meaningful. This is because the column density or abundance ratios will be simply very close to the intensity ratio of the $J = 24 - 23$ (with similar molecular parameters) seen in both isotopologues. This is an order of magnitude higher than what was reported by Araki et al. (2016) in the low-mass star-forming region L1527.

4.6. Deuterations

The deuterium fractionation (D/H ratio) has been suggested as an indicator of the gas temperature in (low-mass) star formation. This D/H ratio is in general anticorrelated with the temperature during the cold prestellar phase (Roberts & Millar 2000; Persson et al. 2018). The deuterium fractionation then decreases through the protostellar evolution (Taquet et al. 2014; Bianchi et al. 2017). Our measurements of D/H from H_2CO appear to follow this trend because the [D_2CO]/[H_2CO] of the hottest source (G211) is the smallest. The [D_2CO]/[H_2CO] = 0.039, 0.091, 0.089, and 0.112 for G211, G208, G210 and G192, respectively. These values are comparable to those of other hot corinos (e.g., 0.046 in IRAS 4B; Parise et al. 2006), except IRAS 16293–2422 B, which is an order of magnitude lower than the others (see Table 7). Since the temperature of H_2CO in IRAS 16293–2422 B is higher (∼107 K; Persson et al. 2018) compared to the sources we presented, it seemingly suggests that the evolution stage of the sources we presented is in general earlier than that of IRAS 16293–2422 B, which is estimated to be $\sim 10^5$ yr (Persson et al. 2018). We note, however, that deuterated methanol is also detected in G211, and the D/H ratio of methanol ([CH_2DOH]/[CH_3OH]) is 0.27, slightly lower than that of IRAS 16293–2422 B. This trend is the opposite to the case for formaldehyde. The use of D/H for diagnosing or differentiating evolutionary ages of objects thus needs to be applied with caution. We note that correcting for the optical thickness of CH_3OH may further reduce the derived [CH_2DOH]/[CH_3OH] values.

4.7. Sulfur-bearing Molecules

Several sulfur-bearing molecules are commonly detected toward the four sources. They mostly have wide line widths, except for carbon monosulfide ^{13}CS. The abundance ratio [^{13}CS]/[H_2S] is ∼0.02 in all four sources. In Drozdovskaya et al. (2018) and Le Gal et al. (2019), the abundance ratio of sulfur-bearing molecules with respect to CS in IRAS 16293–2422 B and other environments was presented, but the uncertainties made it difficult to make the comparison.

The formation or synthesis processes of those S-bearing molecules remain unclear. Models have proposed that sulfur monoxide SO and sulfur dioxide SO_2 are formed in the gas phase from hydrogen sulfide H_2S and carbonyl sulfide OCS evaporated from grain mantles (Palumbo et al. 1997; Hatchell et al. 1998; Esplugues et al. 2014).

Recently, Luo et al. (2019) presented opposite temperature dependencies in the abundances of carbon–sulfur compounds (e.g., ^{13}CS and OCS) and carbon-free sulfur-bearing species (e.g., H_2S, ^{34}SO, and SO_2) in the Orion KL region. Unfortunately, our sample of four hot corinos is too small to investigate these effects within the Orion Molecular Cloud, and larger observational samples are required (Le Gal et al. 2019).

4.8. Trends and Comparisons

Toward the four targets, tracers like CO and SiO show the broadest line widths, clearly marking energetic outflow activities. While COM emissions are not spatially resolved, their line widths are wide, which is especially true for CH_3OH. Lee et al. (2017, 2019) imaged with ALMA a set of COM emissions from the atmosphere of a Keplerian rotating disk around the central YSO. All four sources we are studying, as alluded to earlier, are associated with molecular outflows. They therefore could have circumstellar disks that mediate the accretion and the launching of the outflows. It is tempting to speculate if the COMs we detected are of a similar origin. If the line widths are really a result of rotating motion in the putative circumstellar disks, the broader line widths of CH_3OH suggest that it could originate from the inner part of an incipient disk, as compared to, for example, H_2CO. This is in general consistent with the rotational temperature of CH_3OH being higher than that of H_2CO. On the other hand, the very presence of the outflows also implies the alternative possibility that our observed COMs like CH_3OH are in fact related to the shock activities at the very base of the molecular outflows in the vicinity of the central YSO.

Hydrocarbon and long-carbon-chain species such as CCD, c-C_3H_2, and HCCCN have relatively lower rotational

temperatures and narrower line widths. Such characteristics, which are similar to those of CCH in the hot corino B335 (Imai et al. 2016), indicate that these species are more extended as compared to the continuum and COMs (e.g., c-C_3H_2 in Figure 1). The line profile of CCH in B335 in fact hinted at the existence of double-peak signatures that are due to absorption by the cold envelope gas. We unfortunately are not able to discriminate such features in our study at this stage because of the limited spatial and spectral resolution of the data analyzed. Another species that in general bears a narrow line width is formylium DCO^+.

Among the four hot corino objects, the line widths (Δv) of molecular emission in G208 are overall narrower than those of the other three sources. For CH_3OH as an example, Δv is $\sim$7.5 km s^{-1} in G211, G210, and G192. In contrast, Δv in G208 is 2.3 km s^{-1}. Meanwhile, the lower bolometric temperature in G208 would indicate a smaller region where CH_3OH can be evaporated from the icy mantle. The lower velocity at a closer distance may imply a lower mass for the central protostellar object in G208, if CH_3OH emission is tracing rotational motion in the circumstellar disk. Indeed, the relatively low bolometric luminosity, the most compact and likely young molecular outflows, and the highest envelope mass are all qualitatively but coherently suggestive of a younger stage. Alternatively, the compact morphology of the CO outflow emission and the narrower line widths of trace molecules like CH_3OH may result from an outflow-disk/envelope system viewed pole-on. Finally, there is also the possibility that its COM emissions have a different origin instead of tracing a genuine hot corino like the other three objects, hence giving a different [COM]/[CH_3OH].

In our ALMA observation, 72 fields were observed with 48 sources of protostellar nature for their associations with YSOs or molecular outflows (Dutta et al. 2020, in preparation). Among those, we have identified four hot corino sources, a fraction of $\sim$8%, and the three hot corinos found in Orion A are Class 0 HOPS objects. We note that the 8% face value needs to be treated with caution as the sample size is limited and the selection of the initial 72 fields is based on the JCMT SCUBA-2 detections in the PGCC targets, which implies that these sources are likely more embedded in large-scale envelopes. Other investigations of similar kind show different occurrence rates of corino signatures. For example, the observations with ALMA, as part of the recent VLA/ALMA Nascent Disk and Multiplicity (VANDAM) survey, targeting four fields in the Orion Molecular Cloud-2 (OMC2) Far-infrared sources OMC2-FIR4 and OMC2-FIR3, identified eleven 870 μm continuum sources. Among them, eight sources are associated with HOPS objects, and two of them, HOPS 108 in OMC2-FIR4 and HOPS 370 in OMC2-FIR3, are likely harboring hot corinos as well (Tobin et al. 2019). The Continuum And Lines in Young ProtoStellar Objects (CALYPSO) program by IRAM surveyed 16 Class 0 protostellar systems, some with multiple protostars, in nearby clouds and detected compact (nearly all $<$100 au) CH_3OH emission around about one-half of the protostellar objects (Belloche et al. 2020). It further suggested a luminosity threshold of 4 $L_\odot$, above which YSOs in their sample exhibit spectral features from at least one COM, and no COM emission was detected for sources with luminosities lower than 2 $L_\odot$. They attributed this, though, to the sensitivity of the observations instead of the intrinsic property of the sources with lower luminosities and noted that there exist other COM-detected sources fainter than 2 $L_\odot$ (e.g., $\sim$0.7 $L_\odot$ in B1-bS and $\sim$0.7 $L_\odot$ in B335; Hirano & Liu 2014; Evans et al. 2015). In our study, three hot corinos, of which the spectral energy distributions have been established by Furlan et al. (2016), have luminosities well above that threshold. The luminosity of the fourth source (G192) is at a level of $\sim$14 $L_\odot$ (Dutta et al. 2020, in preparation). There are, on the other hand, protostellar objects in our sample with luminosities much greater than 4 $L_\odot$ but that show no clear sign of hot corinos. It remains unclear whether a hot corino is an evolutionary stage that YSOs would generally experience, or whether only YSOs with certain properties or in certain environments would develop into hot corinos. A full census of YSOs in different environments and evolutionary stages will help in revealing the prevalence of hot corinos and addressing the above questions on a statistical basis.

5. Conclusions

1. Based on a survey toward selected PGCC samples in Orion Molecular Cloud Complex nebula A and B and λ Orionis, we report the detection of four hot corinos based on the presence of warm, compact CH_3OH emission in the four sources and additional COMs in two of them. Given the positional association of their 1.3 mm continuum, three of these four sources are identified as Class 0 YSOs associated with HOPS sources, and the remaining one is for the first time identified as a protostellar core. Further studies with higher angular and spectral resolutions would help to solidify (or falsify) the classification of hot corinos.
2. Some fractional column densities of COMs with respect to methanol, [COM]/[CH_3OH], are an order of magnitude higher than those in other hot corinos in the literature. In G211.47–19.27S, the $^{12}C/^{13}C$ ratio of methanol ([CH_3OH]/[$^{13}CH_3OH$]) is $\sim$10, which is comparable to the values in other hot corinos in the literature. This $^{12}C/^{13}C$ ratio is lower than is typical in the ISM ($\sim$70). The estimated column densities could be affected by beam dilution because the COM emission is not resolved. In addition, the relative abundances with respect to methanol, as well as the $^{12}C/^{13}C$ ratio in CH_3OH, may be affected by its opacity. Variations between hot corinos are in any case expected because of the chemical diversity found in the literature (Bergner et al. 2019).
3. In G211.47–19.27S, both NH_2CHO, a prebiotic molecule, and HNCO are detected. Their estimated column densities are $\sim$3.6 $\times$ 10^{14} cm^{-2} and $\sim$1.2 $\times$ 1015 cm^{-2}, respectively. The abundance ratio [NH_2CHO]/[HNCO] is about twice the estimation based on López-Sepulcre et al. (2015). HNCO is also detected in G210.49–19.79W and G192.12–11.10 without the detection of NH_2CHO. The lack of detection of NH_2CHO may result from the limitation of its low abundance.
4. The D/H ratios of formaldehyde ([D_2CO]/[H_2CO]) of these four sources are in general negatively correlated to their excitation temperatures. These [D_2CO]/[H_2CO], as well as the D/H ratio of methanol ([CH_2DOH]/[CH_3OH]) in G211.47–19.27S, are comparable to those of other hot corinos in the literature except the [D_2CO]/[H_2CO] in IRAS 16293–2422 B. This may result from the difference in either their temperatures or their

evolutionary stages. Note that the D/H ratio of methanol ([CH2DOH]/[CH_3OH]) is also possibly affected by the optical thickness of CH_3OH emission.

5. The hydrocarbons c-C_3H_2 and CCD are also detected in the four sources. They have cooler excitation temperatures and show more extended spatial distributions compared to COMs. HCCCN is detected in all four sources, and its isotope $HC^{13}CCN$ is detected in G211.47–19.27S. The ratio [$HC^{13}CCN$]/[HCCCN] is an order of magnitude higher than the value in the low-mass star-forming region L1527.
6. About 8% of the protostellar objects in our survey are identified as hot corinos. A more complete study of protostellar cores is required to reveal whether a hot corino is a general stage of low-mass star formation.

This paper makes use of the following ALMA data: ADS/JAO.ALMA#2018.1.00302.S. ALMA is a partnership of ESO (representing its member states), NSF (USA), and NINS (Japan), together with NRC (Canada), MOST and ASIAA (Taiwan), and KASI (Republic of Korea), in cooperation with the Republic of Chile. The Joint ALMA Observatory is operated by ESO, AUI/NRAO, and NAOJ. S.Y.H. and S.Y.L. acknowledge support from the Ministry of Science and Technology (MoST) with grants 108-2112-M-001-048- and 108-2112-M-001-052-. N.H. acknowledges support from the Ministry of Science and Technology (MoST) with grant 108-2112-M-001-017. We thank Neal J. Evans and Siyi Feng for their useful comments in improving the manuscript. J.H. thanks the National Natural Science Foundation of China under grant Nos. 11873086 and U1631237 and support by the Yunnan Province of China (No. 2017HC018). This work is sponsored (in part) by the Chinese Academy of Sciences (CAS) through a grant to the CAS South America Center for Astronomy (CASSACA) in Santiago, Chile. C.W.L. is supported by the Basic Science Research Program through the National Research Foundation of Korea (NRF) funded by the Ministry of Education, Science and Technology (NRF-2019R1A2C1010851). D.J. is supported by the National Research Council Canada and by an NSERC Discovery Grant. L.B. acknowledges support from CONICYT project Basal AFB-170002. P.S. was partially supported by a Grant-in-Aid for Scientific Research (KAKENHI Number 18H01259) from the Japan Society for the Promotion of Science (JSPS). Y.-L.Y. was supported, in part, by the Virginia Initiative on Cosmic Origins (VICO). J.E.L. and H.W.Y. are supported by the Basic Science Research Program through the National Research Foundation of Korea (grant No. NRF-2018R1A2B6003423) and the Korea Astronomy and Space Science Institute under the R&D program supervised by the Ministry of Science, ICT and Future Planning.

Software: astropy (Astropy Collaboration et al. 2013; Price-Whelan et al. 2018), CASA (McMullin 2007), XCLASS (Möller et al. 2017).

Appendix A
Observed Spectra of Sources

The spectra of all four sources are presented in Figures A1 to A4; the *x*-axis is the observed frequency. The red curve is the simulation result of XCLASS. Tentative detections are indicated with molecule names in brackets. The frequency bandwidth of each figure is 1 GHz for G211.47–19.27S and G208.68–19.20N1, and 2 GHz in G210.49–19.79W and G192.12–11.10.

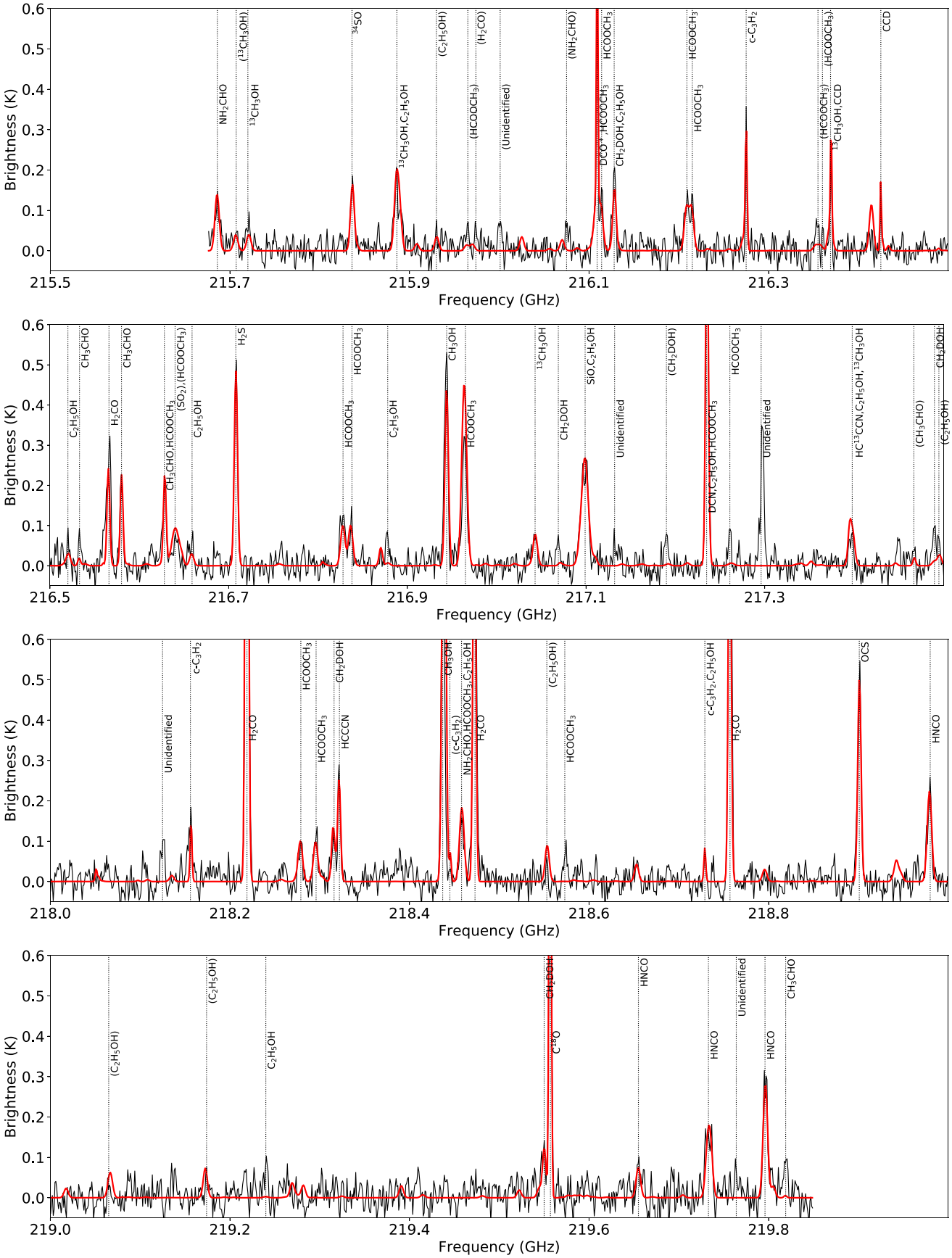

Figure A1. Spectra of G211.47–19.27S.

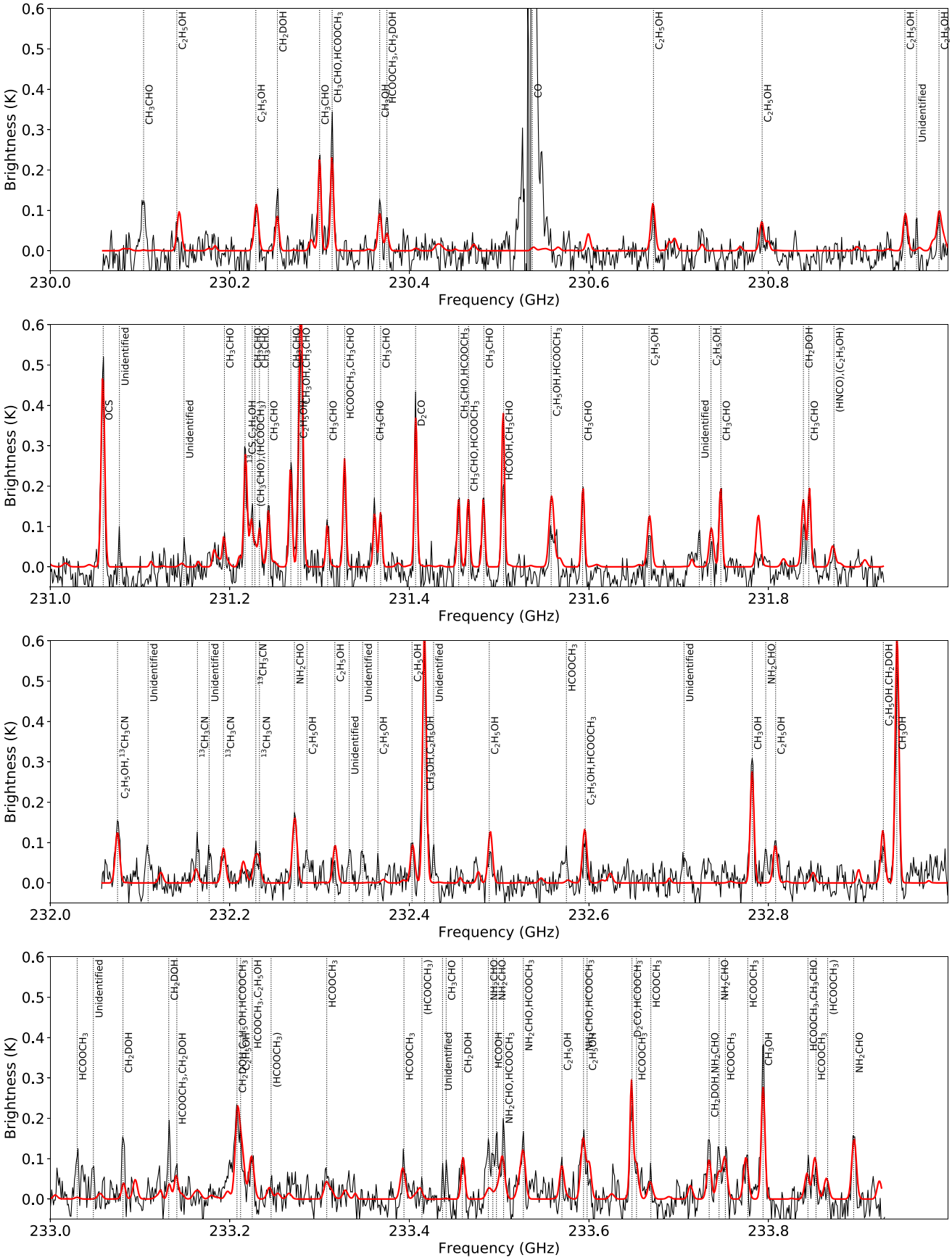

Figure A1. (Continued.)

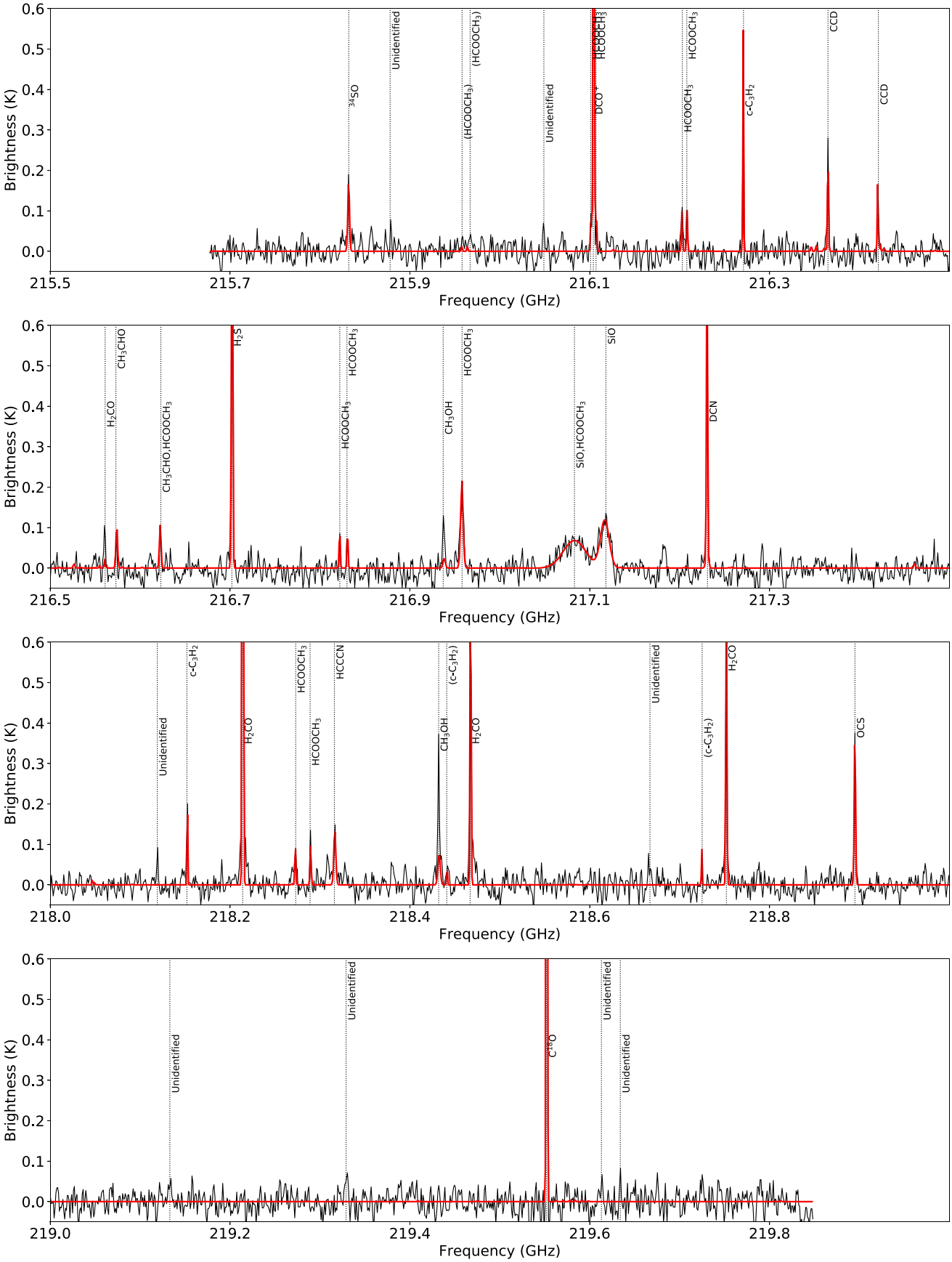

Figure A2. Spectra of G208.68–19.20N1.

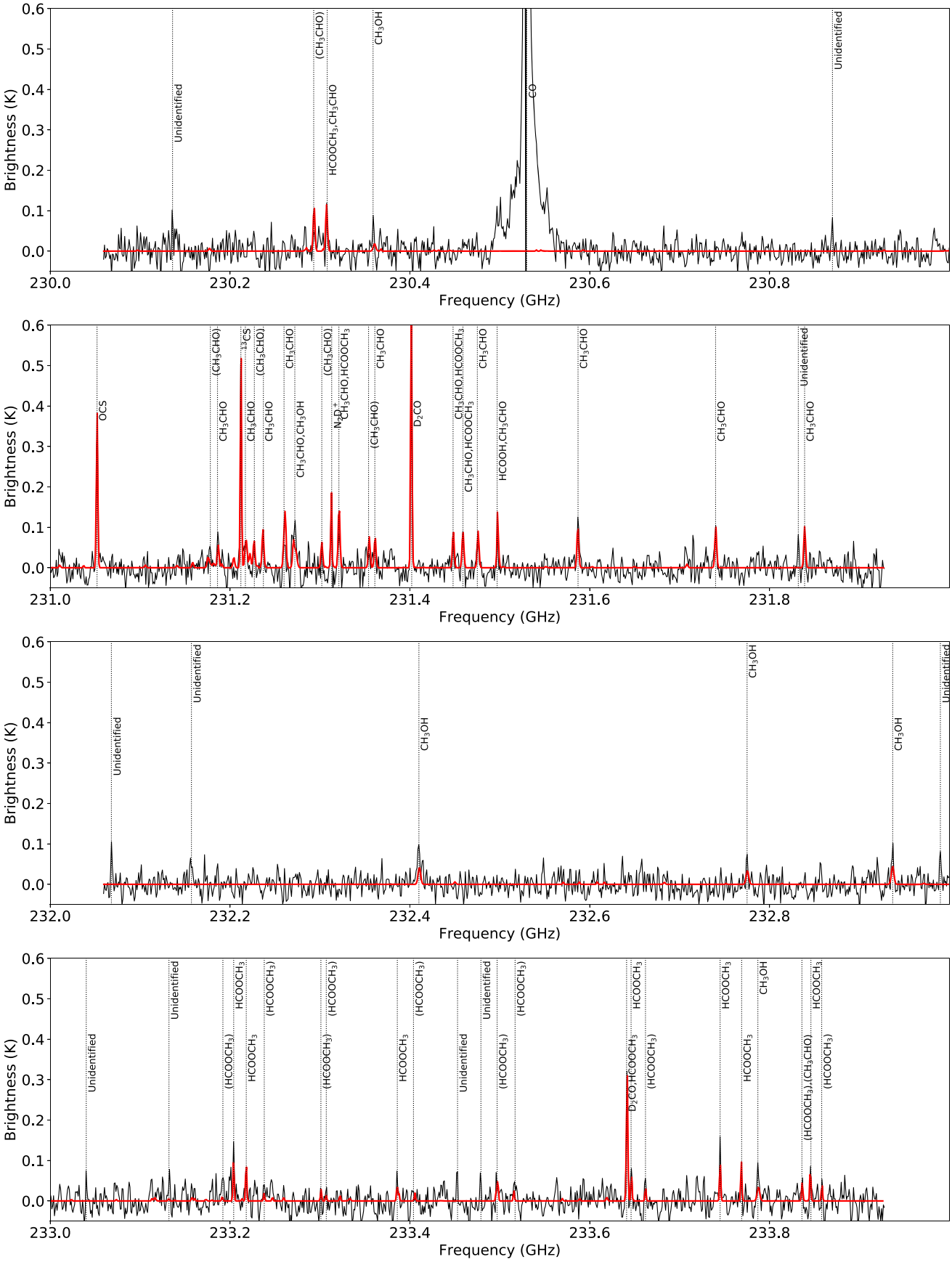

Figure A2. (Continued.)

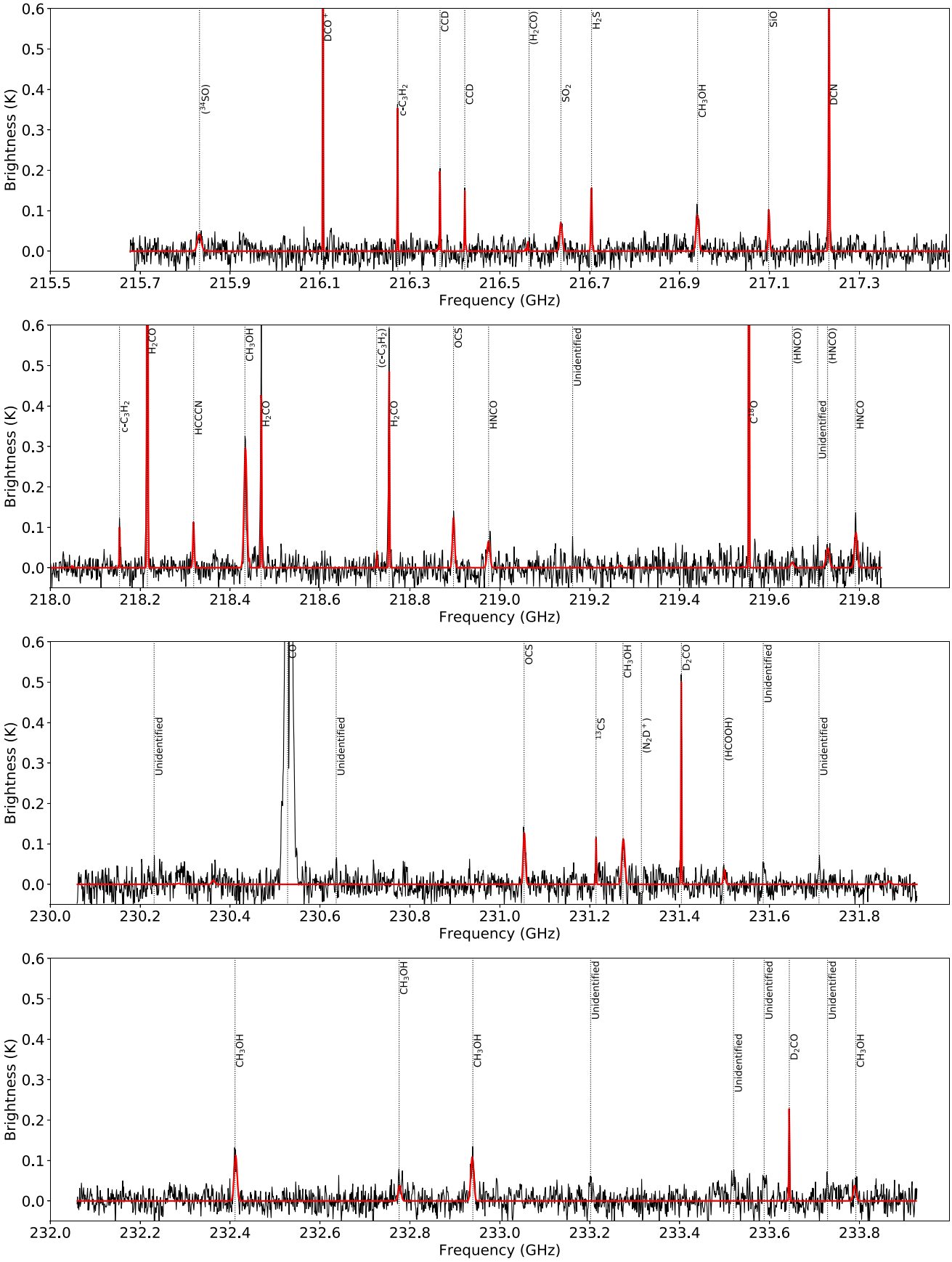

Figure A3. Spectra of G210.49–19.79W.

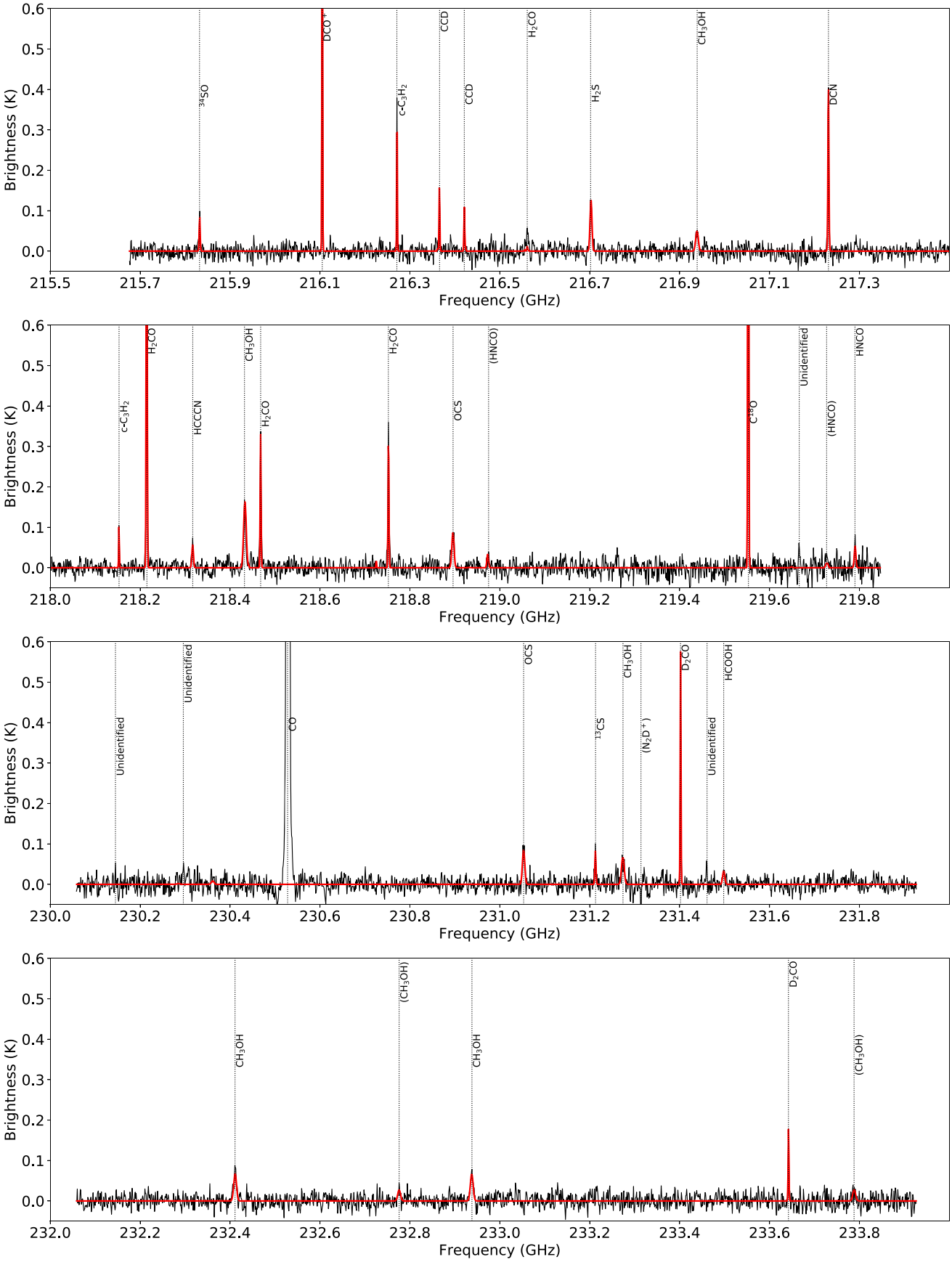

Figure A4. Spectra of G192.12–11.10.

Appendix B
Molecular Line List

Detected transitions of all four sources are presented in Tables B1 to B4. The f^{obs} is the observed frequency, T_p is the peak brightness temperature, Δv is the FWHM line width, and W is the integrated brightness within the FWHM of each line. In the Formula column, the rest frequencies in MHz are provided in brackets. It is denoted as "$^*N$" if there

Table B1
Molecular Line List of G211.47–19.27S

f^{obs} (MHz)	T_p (K)	Δv (km s^{-1})	W (K km s^{-1})	Formula [f^{rest}] (MHz)	Note
215686	0.14	6.95	0.79	NH_2CHO[215688]	
215707	0.05	4.17	0.18	$^{13}CH_3OH$[215708]	T
215720	0.09	4.17	0.3	$^{13}CH_3OH$[215722]	UE
215836	0.17	7.03	0.97	^{34}SO[215840]	
215886	0.18	6.94	1.01	$^{13}CH_3OH$[215887]; C_2H_5OH[215890]	B
215930	0.07	2.78	0.16	C_2H_5OH[215932]	T
215965	0.07	2.78	0.16	$HCOOCH_3$[215966]	T
215974	0.07	2.78	0.16	H_2CO[215976]	T
216001	0.07	5.55	0.31	Unidentified	T, U
216075	0.07	2.29	0.13	NH_2CHO[216077]	T
216109	0.79	2.74	1.75	DCO^+[216113]; $HCOOCH_3$[216110]	B
216114	0.16	4.16	0.54	$HCOOCH_3$[216115, 216116]	B
216128	0.21	5.2	0.88	CH_2DOH[216130]; C_2H_5OH[216127*2]	B
216209	0.13	8.56	0.9	$HCOOCH_3$[216211]	
216215	0.13	6.17	0.65	$HCOOCH_3$[216217]	
216275	0.36	2.23	0.65	c-C_3H_2[216279]	
216355	0.07	3.79	0.21	$HCOOCH_3$[216355]	T
216360	0.05	2.77	0.12	$HCOOCH_3$[216360]	T
216369	0.23	2.92	0.54	$^{13}CH_3OH$[216370]; CCD[216373*3]	B
216425	0.12	2.39	0.23	CCD[216428*2, 216429]	B
216520	0.11	2.77	0.24	C_2H_5OH[216522]	UE
216533	0.11	2.77	0.24	CH_3CHO[216534]	UE
216566	0.27	6.92	1.51	H_2CO[216569]	
216580	0.24	5.09	0.99	CH_3CHO[216582]	
216628	0.22	5.17	0.92	CH_3CHO[216630]; $HCOOCH_3$[216631]	B
216640	0.07	6.92	0.39	SO_2[216643]; $HCOOCH_3$[216638]	T, B
216659	0.09	2.77	0.2	C_2H_5OH[216660]	UE
216708	0.5	5.51	2.23	H_2S[216710]	
216828	0.12	6.91	0.67	$HCOOCH_3$[216830]	
216838	0.14	2.77	0.31	$HCOOCH_3$[216839]	
216878	0.08	4.15	0.27	C_2H_5OH[216879]	UE
216944	0.5	6.91	2.8	CH_3OH[216946]	
216965	0.33	7.06	1.89	$HCOOCH_3$[216963, 216964, 216965, 216966*2, 216967, 216968, 216969]	B
217043	0.09	6.91	0.5	$^{13}CH_3OH$[217045]	
217069	0.08	4.14	0.27	CH_2DOH[217072]	UE
217099	0.27	11.05	2.42	SiO[217105]; C_2H_5OH[217100]	B
217132	0.09	0.94	0.07	Unidentified	U
217190	0.07	5.52	0.32	CH_2DOH[217190]	T
217235	0.89	5.33	3.84	DCN[217237, 217238*2, 217239*2, 217241]; C_2H_5OH[217236, 217238*2]; $HCOOCH_3$[217236]	B
217261	0.1	5.52	0.44	$HCOOCH_3$[217263]	UE
217296	0.36	5.7	1.66	Unidentified	U
217398	0.09	4.39	0.32	$HC^{13}CCN$[217399]; C_2H_5OH[217400]; $^{13}CH_3OH$[217400]	B
217467	0.03	5.51	0.13	CH_3CHO[217469]	T
217490	0.11	5.51	0.48	CH_2DOH[217492]	UE
217495	0.07	4.14	0.22	C_2H_5OH[217497*2]	T, B
218125	0.12	4.12	0.39	Unidentified	U
218156	0.16	5.94	0.77	c-C_3H_2[218160]	
218219	2.58	4.49	9.38	H_2CO[218222]	
218279	0.11	5.49	0.49	$HCOOCH_3$[218281]	
218296	0.12	5.49	0.53	$HCOOCH_3$[218298]	
218316	0.11	5.97	0.53	CH_2DOH[218316]	
218322	0.29	4.24	1.0	HCCCN[218325]	
218437	0.94	5.9	4.49	CH_3OH[218440]	
218445	0.05	2.74	0.11	c-C_3H_2[218449*2]	T, B
218458	0.16	6.31	0.82	NH_2CHO[218460]; $HCOOCH_3$[218458]; C_2H_5OH[218461]	B
218473	1.19	5.49	5.29	H_2CO[218476]	

Table B1
(Continued)

f^{obs} (MHz)	T_p (K)	Δv (km s^{-1})	W (K km s^{-1})	Formula [f^{rest}] (MHz)	Note
218553	0.07	2.69	0.15	C_2H_5OH[218554]	T
218573	0.1	4.11	0.33	$HCOOCH_3$[218575]	UE
218729	0.08	3.53	0.23	c-C_3H_2[218733*2]; C_2H_5OH[218729]	B
218757	1.15	5.77	5.37	H_2CO[218760]	
218901	0.52	5.37	2.26	OCS[218903]	
218980	0.24	5.89	1.15	HNCO[218981]	
219065	0.05	2.74	0.11	C_2H_5OH[219067, 219069]	T, B
219174	0.07	2.74	0.16	C_2H_5OH[219174]	T
219240	0.1	4.1	0.33	C_2H_5OH[219241*2]	B, UE
219550	0.18	2.73	0.4	CH_2DOH[219551]	
219557	1.84	3.42	5.1	$C^{18}O$[219560]	
219655	0.09	5.82	0.42	HNCO[219657*2]	B
219733	0.18	10.91	1.59	HNCO[219734, 219737]	B
219764	0.09	2.73	0.2	Unidentified	U
219796	0.27	8.18	1.79	HNCO[219798]	
219819	0.12	5.46	0.52	CH_3CHO[219820]	UE
230104	0.13	5.21	0.53	CH_3CHO[230106]	UE
230141	0.07	1.6	0.09	C_2H_5OH[230145]	
230229	0.09	6.51	0.47	C_2H_5OH[230231]	
230253	0.15	4.11	0.5	CH_2DOH[230254]	
230300	0.24	5.35	1.04	CH_3CHO[230302]	
230314	0.31	4.96	1.25	CH_3CHO[230316]; $HCOOCH_3$[230316]	B
230367	0.12	6.38	0.62	CH_3OH[230369]	
230375	0.09	3.85	0.28	$HCOOCH_3$[230377]; CH_2DOH[230377]	B, UE
230537	…	…	…	CO[230538]	I
230672	0.11	3.27	0.29	C_2H_5OH[230673]	
230793	0.08	1.89	0.12	C_2H_5OH[230794*2]	B
230952	0.07	5.19	0.29	C_2H_5OH[230954]	
230965	0.09	2.6	0.19	Unidentified	U
230990	0.08	3.89	0.25	C_2H_5OH[230991]	
231059	0.52	5.11	2.15	OCS[231061]	
231077	0.1	0.85	0.07	Unidentified	U
231149	0.07	2.59	0.15	Unidentified	U
231194	0.09	2.74	0.2	CH_3CHO[231195, 231196]	B
231217	0.32	3.89	1.01	^{13}CS[231221]; C_2H_5OH[231221]	B
231225	0.15	3.51	0.43	CH_3CHO[231226, 231227*2]	B
231228	0.06	6.38	0.31	CH_3CHO[231231]; $HCOOCH_3$[231232]	T, B
231233	0.11	4.36	0.39	CH_3CHO[231235*2]	B
231243	0.17	4.01	0.55	CH_3CHO[231245*2]	B
231268	0.26	5.05	1.06	CH_3CHO[231268, 231270*2]	B
231276	0.21	3.55	0.6	C_2H_5OH[231277*2]	B
231279	0.52	6.58	2.77	CH_3OH[231281]; CH_3CHO[231279]	B
231309	0.11	5.18	0.46	CH_3CHO[231310]	
231328	0.25	3.78	0.77	$HCOOCH_3$[231331]; CH_3CHO[231330*2]	B
231361	0.16	4.24	0.55	CH_3CHO[231363]	
231368	0.12	5.18	0.5	CH_3CHO[231370]	
231407	0.41	3.89	1.29	D_2CO[231410]	
231455	0.14	5.18	0.59	CH_3CHO[231457]; $HCOOCH_3$[231457]	B
231466	0.16	4.61	0.6	CH_3CHO[231468]; $HCOOCH_3$[231470]	B
231483	0.18	4.01	0.58	CH_3CHO[231484]	
231505	0.21	3.66	0.62	HCOOH[231506]; CH_3CHO[231506]	B
231558	0.09	6.61	0.48	C_2H_5OH[231559, 231561]; $HCOOCH_3$[231560, 231561]	B
231593	0.19	4.66	0.72	CH_3CHO[231595]	
231667	0.08	3.88	0.25	C_2H_5OH[231669]	
231723	0.08	1.69	0.11	Unidentified	U
231736	0.07	3.37	0.19	C_2H_5OH[231738]	
231747	0.23	5.17	0.96	CH_3CHO[231749]	
231839	0.11	3.81	0.34	CH_2DOH[231840, 231841]	B
231845	0.19	5.18	0.8	CH_3CHO[231848]	
231873	0.06	2.63	0.13	HNCO[231873]; C_2H_5OH[231874*2]	T, B
232075	0.15	7.82	0.95	C_2H_5OH[232076]; $^{13}CH_3CN$[232077*2]	B
232109	0.09	5.17	0.38	Unidentified	U
232164	0.12	5.17	0.49	$^{13}CH_3CN$[232164]	UE

Table B1
(Continued)

f^{obs} (MHz)	T_p (K)	Δv (km s^{-1})	W (K km s^{-1})	Formula [f^{rest}] (MHz)	Note
232177	0.07	6.46	0.38	Unidentified	U
232193	0.07	7.75	0.44	$^{13}CH_3CN$[232195*2]	B
232229	0.09	3.7	0.27	$^{13}CH_3CN$[232230]	
232233	0.09	2.58	0.19	$^{13}CH_3CN$[232234]	
232272	0.18	6.45	0.94	NH_2CHO[232274]	
232286	0.08	3.41	0.22	C_2H_5OH[232287]	UE
232317	0.07	2.09	0.12	C_2H_5OH[232318]	
232333	0.09	3.87	0.28	Unidentified	U
232348	0.09	3.87	0.28	Unidentified	U
232365	0.08	1.29	0.08	C_2H_5OH[232367]	UE
232403	0.11	3.87	0.34	C_2H_5OH[232405]	
232417	0.57	6.04	2.79	CH_3OH[232419]; C_2H_5OH[232423]	B
232427	0.1	1.29	0.11	Unidentified	U
232489	0.09	5.16	0.38	C_2H_5OH[232491]	
232575	0.08	3.87	0.24	$HCOOCH_3$[232579]	UE
232596	0.11	4.38	0.39	C_2H_5OH[232597]; $HCOOCH_3$[232597]	B
232706	0.09	3.86	0.28	Unidentified	U
232782	0.31	6.0	1.51	CH_3OH[232784]	
232797	0.09	3.86	0.28	NH_2CHO[232798]	UE
232808	0.11	5.67	0.51	C_2H_5OH[232809]	
232928	0.09	4.33	0.32	C_2H_5OH[232928]; CH_2DOH[232929]	B
232943	0.59	5.15	2.46	CH_3OH[232945]	
233030	0.13	3.86	0.39	$HCOOCH_3$[233033]	UE
233048	0.09	3.86	0.28	Unidentified	U
233081	0.15	3.86	0.48	CH_2DOH[233083]	UE
233132	0.19	2.57	0.39	CH_2DOH[233134]	UE
233141	0.09	3.73	0.27	$HCOOCH_3$[233141]; CH_2DOH[233142]	B
233208	0.22	7.96	1.42	CH_2DOH[233210]; C_2H_5OH[233209]; $HCOOCH_3$[233213*2]	B
233212	0.18	3.86	0.56	C_2H_5OH[233215]	
233225	0.12	5.14	0.5	$HCOOCH_3$[233227]; C_2H_5OH[233229*2]	B
233246	0.06	2.57	0.12	$HCOOCH_3$[233247*2]	T, B
233308	0.08	5.14	0.33	$HCOOCH_3$[233310, 233310]	B, UE
233394	0.12	5.14	0.5	$HCOOCH_3$[233395*2, 233397]	B
233414	0.05	2.57	0.1	$HCOOCH_3$[233414]	T
233437	0.09	1.93	0.14	Unidentified	U
233441	0.09	2.57	0.19	CH_3CHO[233443]	UE
233459	0.12	6.42	0.62	CH_2DOH[233461]	
233488	0.15	3.85	0.48	NH_2CHO[233490*2, 233492*2]	B, UE
233493	0.12	3.85	0.37	HCOOH[233493*2]	B, UE
233497	0.16	3.85	0.51	NH_2CHO[233499*2]	B, UE
233505	0.19	4.77	0.73	NH_2CHO[233504*2, 233505*2]; $HCOOCH_3$[233505*2, 233507*2]	B
233527	0.16	5.44	0.71	NH_2CHO[233529*2]; $HCOOCH_3$[233525]	B
233570	0.11	2.97	0.26	C_2H_5OH[233571]	
233594	0.19	4.98	0.77	NH_2CHO[233595, 233596]; $HCOOCH_3$[233598]	B
233598	0.09	2.57	0.19	C_2H_5OH[233602]	
233648	0.23	6.42	1.2	D_2CO[233650]; $HCOOCH_3$[233650]	B
233653	0.08	4.11	0.27	$HCOOCH_3$[233655*2]	B
233669	0.09	2.12	0.15	$HCOOCH_3$[233671]	UE
233734	0.16	4.81	0.62	CH_2DOH[233736]; NH_2CHO[233736]	B
233745	0.16	4.81	0.62	NH_2CHO[233747]	
233752	0.14	3.85	0.44	$HCOOCH_3$[233754]	
233777	0.12	3.85	0.37	$HCOOCH_3$[233778]	
233794	0.39	4.82	1.52	CH_3OH[233796]	
233844	0.1	4.75	0.38	$HCOOCH_3$[233845];CH_3CHO[233845]	B
233853	0.09	3.85	0.28	$HCOOCH_3$[233854*2]	B
233866	0.04	2.65	0.09	$HCOOCH_3$[233867]	T
233895	0.17	5.87	0.81	NH_2CHO[233897]	

Table B2
Molecular Line List of G208.68–19.20N1

f^{obs} (MHz)	T_p (K)	Δv (km s^{-1})	W (K km s^{-1})	Formula [f^{rest}] (MHz)	Note
215832	0.19	2.63	0.4	^{34}SO[215840]	
215878	0.08	1.39	0.09	Unidentified	U
215958	0.04	3.07	0.1	$HCOOCH_3$[215966]	T
215967	0.05	4.16	0.15	$HCOOCH_3$[215976]	T
216049	0.07	2.78	0.16	Unidentified	U
216101	0.07	2.77	0.16	$HCOOCH_3$[216110]	
216104	1.72	2.01	2.81	DCO^+[216113]	
216107	0.07	1.17	0.09	$HCOOCH_3$[216116*2]	B
216203	0.1	4.33	0.34	$HCOOCH_3$[216211]	
216208	0.12	2.0	0.2	$HCOOCH_3$[216217]	
216271	0.54	1.39	0.61	c-C_3H_2[216279]	
216365	0.28	2.15	0.49	CCD[216373*3]	B
216421	0.12	2.17	0.21	CCD[216428*2, 216429, 216430, 216430, 216431]	B
216561	0.11	2.68	0.24	H_2CO[216569]	UE
216573	0.09	1.38	0.1	CH_3CHO[216582]	
216623	0.09	2.77	0.2	CH_3CHO[216630]; $HCOOCH_3$[216631]	B
216702	1.08	2.77	2.42	H_2S[216710]	
216822	0.09	1.64	0.12	$HCOOCH_3$[216830]	
216830	0.09	2.77	0.2	$HCOOCH_3$[216839]	
216937	0.14	4.15	0.45	CH_3OH[216946]	
216958	0.16	7.36	0.93	$HCOOCH_3$[216963, 216964, 216965, 216966*2, 216967, 216968, 216969	B
217083	0.09	21.95	1.6	SiO[217105]; $HCOOCH_3$[217077]	B
217118	0.13	13.01	1.34	SiO[217105]	
217231	0.9	2.07	1.51	DCN[217237, 217238, 217239*3, 217241]	B
218119	0.09	1.37	0.1	Unidentified	U
218152	0.23	2.06	0.38	c-C_3H_2[218160]	
218214	3.47	1.93	5.43	H_2CO[218222]	
218273	0.07	5.41	0.33	$HCOOCH_3$[218281]	
218289	0.14	2.06	0.23	$HCOOCH_3$[218298]	
218316	0.14	4.12	0.48	HCCCN[218325]	
218432	0.36	2.62	0.76	CH_3OH[218440]	
218441	0.05	4.12	0.15	c-C_3H_2[218449*2]	T, B
218467	0.64	2.72	1.41	H_2CO[218476]	
218667	0.07	2.74	0.16	Unidentified	U
218725	0.06	1.37	0.07	c-C_3H_2[218733*2]	T, B
218752	0.64	2.41	1.25	H_2CO[218760]	
218895	0.37	2.26	0.68	OCS[218903]	
219133	0.07	2.74	0.16	Unidentified	U
219329	0.07	4.1	0.24	Unidentified	U
219552	5.25	1.73	7.51	C^{18}O[219560]	
219613	0.07	2.73	0.16	Unidentified	U
219634	0.07	2.05	0.12	Unidentified	U
230136	0.1	1.95	0.16	Unidentified	U
230293	0.05	3.14	0.13	CH_3CHO[230302]	T
230308	0.12	1.92	0.19	$HCOOCH_3$[230316]; CH_3CHO[230316]	B
230359	0.09	2.23	0.17	CH_3OH[230369]	UE
230530	…	…	…	CO[230538]	I
230870	0.08	1.95	0.13	Unidentified	U
231052	0.39	2.34	0.75	OCS[231061]	
231178	0.05	2.59	0.11	CH_3CHO[231184]	T
231186	0.09	2.7	0.2	CH_3CHO[231195*2]	B
231212	0.57	1.93	0.89	^{13}CS[231221]	
231217	0.06	5.31	0.26	CH_3CHO[231226, 231227*2]	B
231227	0.05	2.49	0.09	CH_3CHO[231235*2]	T, B
231237	0.08	2.47	0.15	CH_3CHO[231245*2]	B
231260	0.06	4.25	0.22	CH_3CHO[231268, 231270*2]	B
231272	0.11	4.44	0.4	CH_3CHO[231279]; CH_3OH[231281]	B
231302	0.05	2.59	0.09	CH_3CHO[231310*2]	T, B
231313	0.18	2.15	0.3	N_2D^+[231320*3, 231321*4, 231322]	B
231321	0.09	3.43	0.24	CH_3CHO[231330*2]; $HCOOCH_3$[231331]	B
231354	0.03	6.07	0.14	CH_3CHO[231363]	T
231361	0.06	2.74	0.13	CH_3CHO[231370]	
231402	0.71	2.0	1.15	D_2CO[231410]	

Table B2
(Continued)

f^{obs} (MHz)	T_p (K)	Δv (km s^{-1})	W (K km s^{-1})	Formula [f^{rest}] (MHz)	Note
231448	0.09	1.9	0.13	CH_3CHO[231457]; $HCOOCH_3$[231457]	B
231459	0.09	2.77	0.2	CH_3CHO[231468]; $HCOOCH_3$[231470]	B
231475	0.07	3.58	0.2	CH_3CHO[231484]	
231497	0.09	2.59	0.19	HCOOH[231506]; CH_3CHO[231506]	B
231587	0.12	3.16	0.32	CH_3CHO[231595]	
231740	0.1	3.35	0.26	CH_3CHO[231749]	
231832	0.08	2.59	0.17	Unidentified	U
231839	0.1	1.96	0.15	CH_3CHO[231848]	
232068	0.11	0.86	0.07	Unidentified	U
232157	0.07	2.58	0.15	Unidentified	U
232410	0.1	4.23	0.34	CH_3OH[232419]	
232775	0.09	2.23	0.15	CH_3OH[232784]	
232937	0.09	3.19	0.24	CH_3OH[232945]	
232990	0.08	2.57	0.17	Unidentified	U
233040	0.08	1.93	0.13	Unidentified	U
233132	0.08	1.93	0.13	Unidentified	U
233192	0.06	3.65	0.19	$HCOOCH_3$[233200*2]	T, B
233204	0.15	2.12	0.25	$HCOOCH_3$[233213*2]	B
233218	0.08	2.25	0.15	$HCOOCH_3$[233227]	
233238	0.04	3.22	0.11	$HCOOCH_3$[233247*2]	T, B
233301	0.05	1.29	0.05	$HCOOCH_3$[233310*2]	T, B
233307	0.05	1.53	0.05	$HCOOCH_3$[233316]	T
233386	0.09	1.57	0.11	$HCOOCH_3$[233395*2, 233397]	B, U
233404	0.04	2.57	0.07	$HCOOCH_3$[233414]	T
233453	0.08	1.93	0.13	Unidentified	U
233479	0.08	1.93	0.13	Unidentified	U
233497	0.06	2.93	0.13	$HCOOCH_3$[233505, 233507*2]	T, B
233517	0.04	6.5	0.21	$HCOOCH_3$[233525]	T
233641	0.32	2.24	0.59	D_2CO[233650]; $HCOOCH_3$[233650]	B
233646	0.09	2.36	0.16	$HCOOCH_3$[233655*2]	B
233662	0.06	2.31	0.12	$HCOOCH_3$[233671]	T
233745	0.16	1.97	0.26	$HCOOCH_3$[233754]	
233769	0.07	1.92	0.11	$HCOOCH_3$[233778]	
233787	0.09	3.34	0.24	CH_3OH[233796]	
233836	0.06	1.54	0.08	$HCOOCH_3$[233845]; CH_3CHO[233845]	T, B
233846	0.09	1.85	0.13	$HCOOCH_3$[233854*2]	B
233858	0.06	1.92	0.1	$HCOOCH_3$[233867]	T

are N transitions of the same species at the same rest frequency. Definitions for the Note column are as follows:

1. U: Unidentified transition.
2. I: Line ignored in the fitting. They are CO $J = 2$–1 transitions lacking a Gaussian line profile.
3. N: Negative.
4. T: Tentative detection. Their intensity is below $3\sigma_{Chn}$.
5. B: Blended. They are different transitions of either the same species or different species.
6. UE: Underestimated by XCLASS. The observed brightness temperature is above $3\sigma_{Chn}$ but the brightness temperature calculated by XCLASS is below $2\sigma_{Chn}$. There may be blended and unidentified transitions or other components of molecules.

Table B3
Molecular Line List of G210.49–19.79W

f^{obs} (MHz)	T_p (K)	Δv (km s^{-1})	W (K km s^{-1})	Formula [f^{rest}] (MHz)	Note
215832	0.05	11.11	0.43	^{34}SO[215840]	T
216107	1.12	2.77	2.52	DCO^+[216113]	
216273	0.32	2.77	0.72	c-C_3H_2[216279]	
216367	0.23	2.25	0.41	CCD[216373*3]	B
216422	0.18	2.05	0.29	CCD[216428*2, 216429]	B
216565	0.03	4.24	0.11	H_2CO[216569]	T
216636	0.07	6.92	0.41	SO_2[216643]	
216704	0.16	4.31	0.55	H_2S[216710]	
216940	0.1	8.09	0.91	CH_3OH[216946]	
217098	0.1	4.33	0.48	SiO[217105]	
217232	0.72	3.18	1.86	DCN[217237, 217238, 217239*3, 217241]	B
218154	0.12	3.57	0.33	c-C_3H_2[218160]	
218216	2.15	2.77	4.83	H_2CO[218222]	
218319	0.11	4.78	0.43	HCCCN[218325]	
218433	0.32	5.46	1.42	CH_3OH[218440]	
218469	0.56	3.86	1.74	H_2CO[218476]	
218726	0.04	4.11	0.13	c-C_3H_2[218733*2]	T, B
218754	0.58	3.69	1.73	H_2CO[218760]	
218897	0.12	6.85	0.67	OCS[218903]	
218975	0.08	10.95	0.71	HNCO[218981]	
219162	0.08	2.05	0.13	Unidentified	U
219554	3.15	2.73	6.94	C^{18}O[219560]	
219651	0.05	5.46	0.24	HNCO[219657*2]	T, B
219707	0.08	2.05	0.13	Unidentified	U
219729	0.05	5.46	0.24	HNCO[219734*2]	T, B
219791	0.13	5.31	0.54	HNCO[219798]	
230231	0.07	1.3	0.08	Unidentified	U
230528	…	…	…	CO[230538]	I
230636	0.06	3.25	0.17	Unidentified	U
231054	0.13	5.88	0.78	OCS[231061]	
231214	0.12	2.05	0.2	^{13}CS[231221]	
231274	0.11	6.48	0.57	CH_3OH[231281]	
231315	−0.17	2.59	−0.35	N_2D^+[231320]	N
231404	0.55	2.15	0.96	D_2CO[231410]	
231498	0.04	6.01	0.21	HCOOH[231506]	T
231586	0.06	4.51	0.23	Unidentified	U
231710	0.07	5.18	0.28	Unidentified	U
232411	0.12	7.58	0.97	CH_3OH[232419]	
232776	0.09	3.86	0.28	CH_3OH[232784]	
232940	0.1	10.14	1.08	CH_3OH[232945]	
233202	0.07	5.14	0.28	Unidentified	U
233520	0.08	6.42	0.42	Unidentified	U
233588	0.07	6.42	0.37	Unidentified	U
233644	0.22	2.87	0.51	D_2CO[233650]	
233729	0.07	3.21	0.18	Unidentified	U
233792	0.07	3.85	0.22	CH_3OH[233796]	UE

Table B4
Molecular Line List of G192.12–11.10.

f^{obs} (MHz)	T_p (K)	Δv (km s^{-1})	W (K km s^{-1})	Formula [f^{rest}] (MHz)	Note
215832	0.09	2.77	0.21	^{34}SO[215840]	
216105	1.37	2.3	2.55	DCO$^+$[216113]	
216271	0.39	2.1	0.66	c-C_3H_2[216279]	
216366	0.15	2.87	0.36	CCD[216373*3]	B
216421	0.11	2.51	0.23	CCD[216428*2, 216429]	B
216561	0.06	6.48	0.29	H_2CO[216569]	UE
216702	0.14	6.92	0.76	H_2S[216710]	
216939	0.05	6.91	0.27	CH_3OH[216946]	
217231	0.41	3.47	1.16	DCN[217237, 217238, 217239*3]	B
218153	0.11	2.32	0.21	c-C_3H_2[218160]	
218215	1.55	3.03	3.8	H_2CO[218222]	
218317	0.06	4.12	0.21	HCCCN[218325]	
218432	0.16	6.01	0.76	CH_3OH[218440]	
218468	0.33	3.94	1.04	H_2CO[218476]	
218752	0.34	3.82	1.06	H_2CO[218760]	
218896	0.08	8.22	0.53	OCS[218903]	
218975	0.04	2.74	0.09	HNCO[218981]	T
219553	3.68	2.62	7.8	C^{18}O[219560]	
219666	0.05	4.09	0.18	Unidentified	U
219727	0.03	7.11	0.2	HNCO[219737]	T
219790	0.08	3.2	0.2	HNCO[219798]	
230145	0.05	1.95	0.09	Unidentified	U
230296	0.05	3.91	0.17	Unidentified	U
230528	…	…	…	CO[230538]	I
231053	0.09	6.11	0.55	OCS[231061]	
231213	0.09	2.75	0.21	^{13}CS[231221]	
231274	0.07	7.13	0.42	CH_3OH[231281]	
231314	−0.11	1.61	−0.18	N_2D^+[231320]	N
231402	0.57	2.62	1.21	D_2CO[231410]	
232411	0.1	6.45	0.5	CH_3OH[232419]	
231461	0.05	3.89	0.17	Unidentified	U
231498	0.04	6.13	0.18	HCOOH[231506]	T
232776	0.04	3.52	0.12	CH_3OH[232784]	T
232938	0.07	6.51	0.48	CH_3OH[232945]	
233642	0.17	2.86	0.4	D_2CO[233650]	
233788	0.02	12.08	0.2	CH_3OH[233796]	T

Appendix C
Transition List

Table C1 lists the information of the all the detected transitions.

Table C1
List of Identified Transitions

Name	Formula	f_{rest} (MHz)	Transition Number	E_u (K)	g_u	A_u (s^{-1})	$I_{CDMS.JPL}$	Reference
Acetaldehyde	CH_3CHO	216534	14(3,11)–14(2,12) E	117.68	58	3.45e−05	−4.3787	JPL
	CH_3CHO	216582	11(1, 10)–10(1, 9) E	64.87	46	3.55e−04	−3.3908	JPL
	CH_3CHO	216630	11(1, 10)–10(1, 9) A	64.81	46	3.55e−04	−3.3908	JPL
	CH_3CHO	217469	14(3, 11)–14(2, 12) A	117.71	58	3.82e−05	−4.3365	JPL
	CH_3CHO	219820	4(2, 3)–3(1, 3) E	1176.53	63	1.28e−07	−5.1	JPL
	CH_3CHO	230106	26(3, 23)–25(4, 22) E	348.37	106	1.41e−05	−4.8651	JPL
	CH_3CHO	230302	12(2, 11)–11(2, 10) A	81.04	50	4.19e−04	−3.3313	JPL
	CH_3CHO	230316	12(2, 11)–11(2, 10) E	81.05	50	4.19e−04	−3.3314	JPL
	CH_3CHO	231195	12(8, 4)–11(8, 3) E	216.41	50	2.43e−04	−3.7663	JPL
	CH_3CHO	231196	12(9, 4)–11(9, 3) E	254.62	50	1.91e−04	−3.9254	JPL
	CH_3CHO	231226	12(7, 5)–11(7, 4) E	182.65	50	2.88e−04	−3.6428	JPL
	CH_3CHO	231227	12(9, 3)–11(9, 2) A	254.53	50	1.91e−04	−3.9253	JPL
	CH_3CHO	231227	12(9, 4)–11(9, 3) A	254.53	50	1.91e−04	−3.9253	JPL
	CH_3CHO	231231	12(8, 5)–11(8, 4) E	216.33	50	2.43e−04	−3.7662	JPL
	CH_3CHO	231235	12(8, 4)–11(8, 3) A	216.30	50	2.43e−04	−3.7662	JPL
	CH_3CHO	231235	12(8, 5)–11(8, 4) A	216.30	50	2.43e−04	−3.7662	JPL
	CH_3CHO	231245	12(7, 5)–11(7, 4) A	182.58	50	2.88e−04	−3.6426	JPL
	CH_3CHO	231245	12(7, 6)–11(7, 5) A	182.58	50	2.88e−04	−3.6426	JPL
	CH_3CHO	231268	12(7, 6)–11(7, 5) E	182.54	50	2.88e−04	−3.6426	JPL
	CH_3CHO	231270	12(6, 7)–11(6, 6) A	153.36	50	3.28e−04	−3.5445	JPL
	CH_3CHO	231270	12(6, 6)–11(6, 5) A	153.36	50	3.28e−04	−3.5445	JPL
	CH_3CHO	231279	12(6, 6)–11(6, 5) E	153.35	50	3.28e−04	−3.5446	JPL
	CH_3CHO	231310	12(6, 7)–11(6, 6) E	153.26	50	3.28e−04	−3.5444	JPL
	CH_3CHO	231330	12(5, 8)–11(5, 7) A	128.61	50	3.62e−04	−3.4663	JPL
	CH_3CHO	231330	12(5, 7)–11(5, 6) A	128.61	50	3.62e−04	−3.4663	JPL
	CH_3CHO	231363	12(5, 7)–11(5, 6) E	128.54	50	3.62e−04	−3.4663	JPL
	CH_3CHO	231370	12(5, 8)–11(5, 7) E	128.51	50	3.62e−04	−3.4662	JPL
	CH_3CHO	231457	12(4, 9)–11(4, 8) A	108.35	50	3.90e−04	−3.4049	JPL
	CH_3CHO	231468	12(4, 8)–11(4, 7) A	108.36	50	3.90e−04	−3.4049	JPL
	CH_3CHO	231484	12(4, 8)–11(4, 7) E	108.29	50	3.90e−04	−3.4048	JPL
	CH_3CHO	231506	12(4, 9)–11(4, 8) E	108.25	50	3.90e−04	−3.4048	JPL
	CH_3CHO	231595	12(3, 10)–11(3, 9) A	92.57	50	4.12e−04	−3.3586	JPL
	CH_3CHO	231749	12(3, 10)–11(3, 9) E	92.51	50	4.09e−04	−3.3615	JPL
	CH_3CHO	231848	12(3, 9)–11(3, 8) E	92.61	50	4.10e−04	−3.3611	JPL
	CH_3CHO	233443	17(2, 16)–17(0, 17) A	149.96	70	2.35e−06	−5.5424	JPL
	CH_3CHO	233845	6(3, 3)–6(2, 4) E	39.81	26	3.51e−05	−4.6399	JPL
Carbon monosulfide (^{13}C-substituted)	^{13}CS	231221	5–4	33.29	22	2.51e−04	−1.6401	CDMS
Carbon monoxide	CO	230538	2–1	16.59	5	6.91e−07	−4.1197	CDMS
Carbon monoxide (^{18}O-substituted)	$C^{18}O$	219560	2–1	15.81	5	6.01e−07	−4.1794	CDMS
Carbonyl sulfide	OCS	218903	3(2, 1)–2(2, 0)	99.81	37	3.04e−05	−3.0903	CDMS
	OCS	231061	19–18	110.90	39	3.58e−05	−2.6263	CDMS
Cyanoacetylene	HCCCN	218325	24–23	130.98	49	8.26e−04	−1.2947	CDMS

Table C1
(Continued)

Name	Formula	f_{rest} (MHz)	Transition Number	E_u (K)	g_u	A_u (s^{-1})	$I_{CDMS.JPL}$	Reference
Cyanoacetylene (^{13}C-substituted)	$HC^{13}CCN$	217399	24–23	130.42	49	8.16e−04	−1.2994	CDMS
Cyclopropenylidene	c-C_3H_2	216279	3(3, 0)–2(2, 1)	19.47	21	2.56e−04	−2.9741	CDMS
	c-C_3H_2	218160	5(2, 4)–4(1, 3)	35.42	11	4.04e−04	−3.0831	CDMS
	c-C_3H_2	218449	8(2, 6)–8(1, 7)	86.93	17	1.49e−04	−3.4013	CDMS
	c-C_3H_2	218449	8(3, 6)–8(2, 7)	86.93	51	1.49e−04	−2.9242	CDMS
	c-C_3H_2	218733	7(1, 6)–7(0, 7)	61.17	15	8.93e−05	−3.1652	CDMS
	c-C_3H_2	218733	7(2, 6)–7(1, 7)	61.17	45	8.93e−05	−3.6423	CDMS
Diazenylium (deuterated)	N_2D^+	231320	3(3, 2)–2(3, 2)	22.20	5	8.82e−05	−3.1516	CDMS
	N_2D^+	231320	3(3, 4)–2(3, 4)	22.20	9	8.30e−05	−2.9226	CDMS
	N_2D^+	231320	3(3, 3)–2(3, 3)	22.20	7	4.55e−05	−3.2931	CDMS
	N_2D^+	231321	3(2, 2)–2(1, 2)	22.20	5	1.39e−04	−2.9555	CDMS
	N_2D^+	231321	3(2, 2)–2(1, 1)	22.20	5	4.31e−04	−2.463	CDMS
	N_2D^+	231321	3(2, 1)–2(1, 0)	22.20	3	3.33e−04	−2.7964	CDMS
	N_2D^+	231321	3(4, 4)–2(3, 4)	22.20	9	3.59e−05	−3.2863	CDMS
	N_2D^+	231322	3(3, 3)–2(2, 3)	22.20	7	9.01e−05	−2.9965	CDMS
	N_2D^+	231322	3(2, 3)–2(1, 2)	22.20	7	6.07e−04	−2.1678	CDMS
	N_2D^+	231322	3(3, 3)–2(2, 2)	22.20	7	5.69e−04	−2.1961	CDMS
	N_2D^+	231322	3–2	22.20	63	4.38e−04	−1.3554	CDMS
	N_2D^+	231322	3(3, 2)–2(2, 1)	22.20	5	5.49e−04	−2.3578	CDMS
	N_2D^+	231322	3(3, 4)–2(2, 3)	22.20	9	6.24e−04	−2.0467	CDMS
	N_2D^+	231322	3(4, 4)–2(3, 3)	22.20	9	6.78e−04	−2.0109	CDMS
	N_2D^+	231322	3(4, 3)–2(3, 2)	22.20	7	6.46e−04	−2.141	CDMS
	N_2D^+	231322	3(4, 5)–2(3, 4)	22.20	11	7.14e−04	−1.9011	CDMS
	N_2D^+	231322	3(2, 1)–2(1, 1)	22.20	3	2.81e−04	−2.8709	CDMS
	N_2D^+	231322	3(3, 2)–2(2, 2)	22.20	5	6.64e−05	−3.2752	CDMS
	N_2D^+	231322	3(4, 3)–2(3, 3)	22.20	7	6.57e−05	−3.1332	CDMS
Ethanol	C_2H_5OH	215890	25(4, 22)t–25(3, 23)t	294.18	51	6.14e−05	⋯	JPL
	C_2H_5OH	215932	11(0, 11)g–10(1, 9)g+	115.30	23	3.09e−05	⋯	JPL
	C_2H_5OH	216127	12(9, 3)t–13(8, 6)t	167.06	25	3.86e−06	⋯	JPL
	C_2H_5OH	216127	12(9, 4)t–13(8, 5)t	167.06	25	3.86e−06	⋯	JPL
	C_2H_5OH	216273	40(5, 35)t–40(4, 36)t	732.02	81	6.21e−05	⋯	JPL
	C_2H_5OH	216416	13(0, 13)g+–12(0, 12)g+	130.63	27	9.08e−05	⋯	JPL
	C_2H_5OH	216522	8(4, 4)g+–7(3, 4)g−	106.30	17	3.48e−05	⋯	JPL
	C_2H_5OH	216660	8(4, 5)g+–7(3, 5)g−	106.30	17	3.48e−05	⋯	JPL
	C_2H_5OH	216879	47(8, 40)g+–47(7, 40)g−	1075.45	95	3.51e−05	⋯	JPL
	C_2H_5OH	217100	45(6, 39)t–45(5, 40)t	927.02	91	6.27e−05	⋯	JPL
	C_2H_5OH	217236	51(1, 51)g+–50(2, 49)g−	1098.44	103	1.69e−05	⋯	JPL
	C_2H_5OH	217238	51(0, 51)g+–50(1, 49)g−	1098.44	103	3.51e−05	⋯	JPL
	C_2H_5OH	217238	40(9, 31)t–39(10, 30)t	791.86	81	1.83e−05	⋯	JPL
	C_2H_5OH	217400	31(6, 26)t–30(7, 23)t	463.51	63	1.96e−05	⋯	JPL
	C_2H_5OH	217497	13(1, 13)g—12(0, 12)g−	134.51	27	3.36e−07	⋯	JPL
	C_2H_5OH	217497	34(5, 29)g+–34(4, 31)g−	586.69	69	3.57e−05	⋯	JPL
	C_2H_5OH	218461	5(3, 2)t–4(2, 3)t	23.89	11	6.60e−05	⋯	JPL
	C_2H_5OH	218554	21(5, 16)t–21(4, 17)t	226.01	43	6.21e−05	⋯	JPL
	C_2H_5OH	218729	56(13, 44)g+–55(14, 42)g−	1590.39	113	1.05e−05	⋯	JPL
	C_2H_5OH	218943	35(4, 31)t–35(3, 32)t	559.69	71	6.47e−05	⋯	JPL
	C_2H_5OH	219067	22(4, 19)g—22(3, 19)g+	292.05	45	3.62e−05	⋯	JPL

Table C1
(Continued)

Name	Formula	f_{rest} (MHz)	Transition Number	E_u (K)	g_u	A_u (s^{-1})	$I_{CDMS.JPL}$	Reference
	C_2H_5OH	219069	32(7, 25)g+–32(6, 27)g−	556.35	65	3.56e−05	···	JPL
	C_2H_5OH	219174	30(3, 27)t–30(2, 28)t	409.96	61	6.51e−05	···	JPL
	C_2H_5OH	219241	52(13, 40)t–51(14, 37)t	1369.56	105	1.78e−05	···	JPL
	C_2H_5OH	219241	52(13, 39)t–51(14, 38)t	1369.56	105	1.78e−05	···	JPL
	C_2H_5OH	230145	25(3, 23)t–25(2, 24)t	283.82	51	7.51e−05	···	JPL
	C_2H_5OH	230231	13(2, 11)g—12(2, 10)g−	143.28	27	1.07e−04	···	JPL
	C_2H_5OH	230673	13(2, 11)g+–12(2, 10)g+	138.62	27	1.07e−04	···	JPL
	C_2H_5OH	230794	6(5, 1)g+–5(4, 1)g−	104.80	13	6.12e−05	···	JPL
	C_2H_5OH	230794	6(5, 2)g+–5(4, 2)g−	104.80	13	6.12e−05	···	JPL
	C_2H_5OH	230954	16(5, 11)t–16(4, 12)t	145.77	33	7.10e−05	···	JPL
	C_2H_5OH	230991	14(0, 14)t–13(1, 13)t	85.53	29	6.87e−05	···	JPL
	C_2H_5OH	230997	41(5, 36)t–41(4, 37)t	767.38	83	7.58e−05	···	JPL
	C_2H_5OH	231221	10(3, 7)g—10(2, 9)g+	118.42	21	4.12e−05	···	JPL
	C_2H_5OH	231277	55(14, 41)t–54(15, 40)t	1538.49	111	2.07e−05	···	JPL
	C_2H_5OH	231277	55(14, 42)t–54(15, 39)t	1538.49	111	2.07e−05	···	JPL
	C_2H_5OH	231559	21(5, 17)t–21(4, 18)t	225.95	43	7.39e−05	···	JPL
	C_2H_5OH	231561	20(5, 16)t–20(4, 17)t	208.21	41	7.36e−05	···	JPL
	C_2H_5OH	231669	14(1, 14)g+–13(1, 13)g+	141.90	29	1.11e−04	···	JPL
	C_2H_5OH	231738	19(5, 15)t–19(4, 16)t	191.32	39	7.33e−05	···	JPL
	C_2H_5OH	231790	31(5, 27)g—31(4, 27)g+	505.98	63	4.30e−05	···	JPL
	C_2H_5OH	231790	22(5, 18)t–22(4, 19)t	244.54	45	7.44e−05	···	JPL
	C_2H_5OH	231841	35(9, 26)g—34(10, 24)g+	684.80	71	1.15e−05	···	JPL
	C_2H_5OH	231874	20(10, 10)g—21(9, 12)g+	358.85	41	6.74e−06	···	JPL
	C_2H_5OH	231874	20(10, 11)g—21(9, 13)g+	358.85	41	6.74e−06	···	JPL
	C_2H_5OH	232076	15(5, 10)t–15(4, 11)t	132.29	31	7.13e−05	···	JPL
	C_2H_5OH	232287	29(4, 26)g—29(3, 27)g−	443.72	59	3.89e−07	···	JPL
	C_2H_5OH	232318	23(5, 19)t–23(4, 20)t	263.99	47	7.52e−05	···	JPL
	C_2H_5OH	232367	33(6, 27)g+–33(5, 28)g+	565.06	67	3.84e−07	···	JPL
	C_2H_5OH	232405	17(5, 13)t–17(4, 14)t	160.10	35	7.30e−05	···	JPL
	C_2H_5OH	232423	43(8, 35)g+–42(9, 33)g−	923.33	87	1.41e−05	···	JPL
	C_2H_5OH	232491	14(0, 14)g+–13(0, 13)g+	141.79	29	1.13e−04	···	JPL
	C_2H_5OH	232597	14(1, 14)g—13(1, 13)g−	146.53	29	1.12e−04	···	JPL
	C_2H_5OH	232809	16(5, 12)t–16(4, 13)t	145.77	33	7.27e−05	···	JPL
	C_2H_5OH	232928	14(5, 9)t–14(4, 10)t	119.66	29	7.11e−05	···	JPL
	C_2H_5OH	233209	24(5, 20)t–24(4, 21)t	284.28	49	7.63e−05	···	JPL
	C_2H_5OH	233215	15(5, 11)t–15(4, 12)t	132.29	31	7.23e−05	···	JPL
	C_2H_5OH	233229	43(20, 24)g+–44(21, 24)g−	1433.18	87	4.86e−05	···	JPL
	C_2H_5OH	233229	43(20, 23)g+–44(21, 23)g−	1433.18	87	4.86e−05	···	JPL
	C_2H_5OH	233571	13(5, 8)t–13(4, 9)t	107.87	27	7.05e−05	···	JPL
	C_2H_5OH	233602	14(5, 10)t–14(4, 11)t	119.65	29	7.17e−05	···	JPL
Ethynyl (deuterated)	CCD	216373	$N = 3$–2, $J = 7/2$–5/2, $F = 9/2$–7/2	20.76	10	3.00e−05	−3.143	CDMS
	CCD	216373	$N = 3$–2, $J = 7/2$-5/2, $F = 5/2$–3/2	20.76	6	2.67e−05	−3.4142	CDMS
	CCD	216373	$N = 3$–2, $J = 7/2$-5/2, $F = 7/2$–5/2	20.76	8	2.76e−05	−3.275	CDMS
	CCD	216428	$N = 3$–2, $J = 5/2$-3/2, $F = 7/2$–5/2	20.78	8	2.78e−05	−3.2724	CDMS
	CCD	216428	$N = 3$–2, $J = 5/2$-3/2, $F = 5/2$–3/2	20.78	6	2.34e−05	−3.4728	CDMS
	CCD	216429	$N = 3$–2, $J = 5/2$-3/2, $F = 3/2$–1/2	20.78	4	2.10e−05	−3.6956	CDMS

Table C1
(Continued)

Name	Formula	f_{rest} (MHz)	Transition Number	E_u (K)	g_u	A_u (s^{-1})	$I_{CDMS.JPL}$	Reference
Formaldehyde	H_2CO	215976	11(2, 9)–12(0, 12)	279.73	23	3.15e−07	−5.5745	CDMS
	H_2CO	216569	9(1, 8)–9(1, 9)	173.99	57	7.22e−06	−3.6678	CDMS
	H_2CO	218222	3(0, 3)–2(0, 2)	20.95	7	2.82e−04	−2.769	CDMS
	H_2CO	218476	3(2, 2)–2(2, 1)	68.10	7	1.57e−04	−3.0914	CDMS
	H_2CO	218760	3(2, 1)–2(2, 0)	68.11	7	1.58e−04	−3.0903	CDMS
Formaldehyde (doubly deuterated)	D_2CO	231410	4(0, 4)–3(0, 3)	27.89	18	3.47e−04	−2.4242	CDMS
	D_2CO	233650	4(2, 3)–3(2, 2)	49.62	18	2.69e−04	−2.5711	CDMS
Formamide	NH_2CHO	215688	10(2, 8)–9(2, 7)	68.45	126	6.98e−04	−2.4894	JPL
	NH_2CHO	216077	15(5, 11)–16(4, 12)	196.78	93	5.62e−06	−4.6007	JPL
	NH_2CHO	218460	10(1, 9)–9(1, 8)	60.81	126	7.48e−04	−2.4541	JPL
	NH_2CHO	232274	11(2, 10)–10(2, 9)	78.95	138	8.82e−04	−2.3953	JPL
	NH_2CHO	232798	20(6, 14)–21(5, 17)	321.27	123	7.34e−06	−4.5759	JPL
	NH_2CHO	233490	11(8, 3)–10(8, 2), $F = 11$-10	257.73	23	4.33e−04	−3.4424	JPL
	NH_2CHO	233490	11(8, 4)–10(8, 3), $F = 11$-10	257.73	23	4.33e−04	−3.4424	JPL
	NH_2CHO	233492	11(9, 2)–10(9, 1), $F = 10$-9	308.24	21	3.04e−04	−3.7092	JPL
	NH_2CHO	233492	11(9, 3)–10(9, 2), $F = 10$-9	308.24	21	3.04e−04	−3.7092	JPL
	NH_2CHO	233493	11(9, 2)–10(9, 1), $F = 11$-10	308.24	23	3.04e−04	−3.6693	JPL
	NH_2CHO	233493	11(9, 3)–10(9, 2), $F = 11$-10	308.24	23	3.04e−04	−3.6693	JPL
	NH_2CHO	233499	11(7, 4)–10(7, 3), $F = 11$-10	213.13	23	5.47e−04	−3.2763	JPL
	NH_2CHO	233499	11(7, 5)–10(7, 4), $F = 11$-10	213.13	23	5.47e−04	−3.2763	JPL
	NH_2CHO	233504	11(10, 1)–10(10, 0), $F = 10$-9	364.65	21	1.59e−04	−4.0706	JPL
	NH_2CHO	233504	11(10, 2)–10(10, 1), $F = 10$-9	364.65	21	1.59e−04	−4.0706	JPL
	NH_2CHO	233505	11(10, 1)–10(10, 0), $F = 11$-10	364.65	23	1.60e−04	−4.0308	JPL
	NH_2CHO	233505	11(10, 2)–10(10, 1), $F = 11$-10	364.65	23	1.60e−04	−4.0308	JPL
	NH_2CHO	233529	11(6, 6)–10(6, 5)	174.45	92	6.51e−04	−2.6674	JPL
	NH_2CHO	233529	11(6, 5)–10(6, 4)	174.45	92	6.51e−04	−2.6674	JPL
	NH_2CHO	233595	11(5, 7)–10(5, 6)	141.71	92	7.36e−04	−2.5669	JPL
	NH_2CHO	233596	11(5, 6)–10(5, 5)	141.71	92	7.36e−04	−2.5669	JPL
	NH_2CHO	233736	11(4, 8)–10(4, 7)	114.93	69	8.07e−04	−2.4887	JPL
	NH_2CHO	233747	11(4, 7)–10(4, 6)	114.93	69	8.07e−04	−2.4887	JPL
	NH_2CHO	233897	11(3, 9)–10(3, 8)	94.11	138	8.62e−04	−2.43	JPL
Formic acid	HCOOH	218939	8(1, 8)–7(0, 7)	40.52	17	2.46e−06	−5.1495	CDMS
	HCOOH	231506	10(1, 9)–9(1, 8)	64.47	21	1.33e−04	−3.1815	CDMS
Formylium (deuterated)	DCO^+	216113	19(2, 18)–18(2, 17) E	20.74	7	7.66e−04	−3.9637	JPL
Hydrogen cyanide (deuterated)	DCN	217237	$J = 3$–2, $F = 3$–3	20.86	7	5.08e−05	−2.7679	JPL
	DCN	217238	$J = 3$–2, $F = 2$–1	20.86	5	3.84e−04	−2.0355	JPL
	DCN	217239	$J = 3$–2, $F = 3$–2	20.86	7	4.07e−04	−1.8648	JPL
	DCN	217239	$J = 3$–2, $F = 4$–3	20.86	21	4.58e−04	−1.7046	JPL
	DCN	217241	$J = 3$–2, $F = 2$–2	20.86	5	7.12e−05	−2.7679	JPL
Hydrogen sulfide	H_2S	216710	2(2, 0)–2(1, 1)	83.98	5	4.87e−05	−3.0171	CDMS
Isocyanic acid	HNCO	218981	10(1, 10)–9(1, 9)	101.08	21	1.42e−04	−2.6771	CDMS
	HNCO	219657	10(3, 8)–9(3, 7)	432.96	21	1.20e−04	−2.6771	CDMS
	HNCO	219657	10(3, 7)–9(3, 6)	432.96	21	1.20e−04	−3.2322	CDMS
	HNCO	219734	10(2, 9)–9(2, 8)	228.29	21	1.35e−04	−2.8867	CDMS
	HNCO	219737	10(2, 8)–9(2, 7)	228.29	21	1.35e−04	−2.8867	CDMS
	HNCO	219798	10(0, 10)–9(0, 9)	58.02	21	1.47e−04	−2.6022	CDMS
	HNCO	231873	28(1, 28)–29(0, 29)	469.87	57	6.68e−05	−3.1298	CDMS

Table C1
(Continued)

Name	Formula	f_{rest} (MHz)	Transition Number	E_u (K)	g_u	A_u (s^{-1})	$I_{CDMS.JPL}$	Reference
Methanol	CH_3OH	216946	5(1, 4)–4(2, 3) E	55.87	44	1.21e−05	−4.5032	JPL
	CH_3OH	218440	4(2, 2)–3(1, 2) E	45.46	36	4.69e−05	−3.9915	JPL
	CH_3OH	230369	22(4, 18)–21(5, 16) E	682.75	180	2.08e−05	−4.5906	JPL
	CH_3OH	231281	10(2, 9)–9(3, 6) A2	165.35	84	1.83e−05	−4.2284	JPL
	CH_3OH	232419	10(2, 8)–9(3, 7) A1	165.40	84	1.87e−05	−4.2242	JPL
	CH_3OH	232784	18(3, 16)–17(4, 13) A1	446.53	148	2.16e−05	−4.3202	JPL
	CH_3OH	232945	10(3, 7)–11(2, 9) E	190.37	84	2.13e−05	−4.2038	JPL
	CH_3OH	233796	18(3, 15)–17(4, 14) A2	446.58	148	2.20e−05	−4.3164	JPL
Methanol (deuterated)	CH_2DOH	216130	12(0, 12)e0-11(1, 11)e1	166.52	25	1.55e−05	−4.269	JPL
	CH_2DOH	217072	3(2, 2)e1–3(2, 1)e0	39.43	7	4.00e−07	−6.2276	JPL
	CH_2DOH	217190	16(1, 16)e1–15(3, 13)e0	304.06	33	9.69e−08	−6.5535	JPL
	CH_2DOH	217492	7(3, 4)e1–8(1, 7)e1	104.88	15	1.42e−08	−7.4418	JPL
	CH_2DOH	218316	5(2, 4)e1–5(1, 5)e1	58.71	11	6.69e−06	−4.8387	JPL
	CH_2DOH	219551	5(1, 5)e1–4(1, 4)e1	48.23	11	5.09e−06	−4.9441	JPL
	CH_2DOH	230254	16(2, 14)e0–16(1, 15)e0	310.21	33	6.50e−05	−3.7605	JPL
	CH_2DOH	230377	15(2, 13)01–15(1, 14)o1	292.77	31	2.28e−05	−4.2186	JPL
	CH_2DOH	231840	10(1, 9)e0–9(2, 8)e0	123.70	21	1.22e−05	−4.4162	JPL
	CH_2DOH	232929	3(3, 0)e0–4(2, 3)e0	48.77	7	3.26e−06	−5.3608	JPL
	CH_2DOH	233083	5(3, 2)e0–4(2, 2)o1	68.10	11	2.33e−06	−5.339	JPL
	CH_2DOH	233134	5(3, 3)e0–4(2, 3)o1	68.09	11	2.35e−06	−5.3351	JPL
	CH_2DOH	233142	5(3, 3)e0–4(2, 3)o1	260.58	29	2.22e−05	−5.3351	JPL
	CH_2DOH	233210	17(2, 15)e0–17(1, 16)e0	347.06	35	6.49e−05	−3.7945	JPL
	CH_2DOH	233461	9(2, 8)e1–9(1, 9)e1	122.94	19	8.68e−06	−4.6097	JPL
	CH_2DOH	233736	7(3, 5)e1–8(2, 6)e0	104.88	15	2.70e−06	−5.1942	JPL
Methanol (^{13}C-substituted)	$^{13}CH_3OH$	215708	8(4, 5)–9(3, 6) A2	162.33	17	1.13e−05	−3.02967	CDMS
	$^{13}CH_3OH$	215722	8(4, 4)–9(3, 7) A1	162.33	17	1.13e−05	−3.02974	CDMS
	$^{13}CH_3OH$	215887	4(2, 2)–3(1, 2) E2	45.01	9	4.53e−05	−2.53306	CDMS
	$^{13}CH_3OH$	216370	10(2, 9)–9(3, 6) A2	162.36	21	1.50e−05	−2.81704	CDMS
	$^{13}CH_3OH$	217045	14(1, 13)–13(2, 12) A2	254.26	29	2.37e−05	−2.61267	CDMS
	$^{13}CH_3OH$	217400	10(2, 8)–9(3, 7) A1	162.41	21	1.53e−05	−2.81298	CDMS
Methyl cyanide (^{13}C-substituted)	$^{13}CH_3CN$	232077	13(6)A1–12(6)A2	335.51	54	8.48e−04	⋯	CDMS
	$^{13}CH_3CN$	232077	13(6)A2–12(6)A1	335.51	54	8.48e−04	⋯	CDMS
	$^{13}CH_3CN$	232164	13(4)E–12(4)E	192.50	54	9.76e−04	⋯	CDMS
	$^{13}CH_3CN$	232195	13(3)A2–12(3)A1	142.42	54	1.02e−03	⋯	CDMS
	$^{13}CH_3CN$	232195	13(3)A1-12(3)A2	142.42	54	1.02e−03	⋯	CDMS
	$^{13}CH_3CN$	232217	13(2)E–12(2)E	106.65	54	1.05e−03	⋯	CDMS
	$^{13}CH_3CN$	232230	13(1)E–12(1)E	85.18	54	1.07e−03	⋯	CDMS
	$^{13}CH_3CN$	232234	13(0)A2–12(0)A1	78.03	54	1.08e−03	⋯	CDMS
Methyl formate	$HCOOCH_3$	215966	19(1, 18)–18(2, 17) E	109.33	78	1.96e−05	−4.8434	JPL
	$HCOOCH_3$	216110	19(2, 18)–18(2, 17) E	109.34	78	1.49e−04	−3.9637	JPL
	$HCOOCH_3$	216115	29(9, 20)–29(8, 21) A	311.99	118	1.51e−05	−5.0697	JPL
	$HCOOCH_3$	216116	19(2, 18)–18(2, 17) A	109.32	78	1.49e−04	−3.9636	JPL
	$HCOOCH_3$	216211	19(1, 18)–18(1, 17) E	109.34	78	1.49e−04	−3.9632	JPL
	$HCOOCH_3$	216217	19(1, 18)–18(1, 17) A	109.32	78	1.49e−04	−3.9631	JPL
	$HCOOCH_3$	216355	19(2, 18)–18(1, 17) E	109.34	78	1.97e−05	−4.8417	JPL
	$HCOOCH_3$	216360	19(2, 18)–18(1, 17) A	109.32	78	1.97e−05	−4.8419	JPL
	$HCOOCH_3$	216631	36(8, 29)–36(7, 30) E	440.47	146	1.53e−05	−5.1583	JPL

Table C1
(Continued)

Name	Formula	f_{rest} (MHz)	Transition Number	E_u (K)	g_u	A_u (s^{-1})	$I_{CDMS.JPL}$	Reference
	$HCOOCH_3$	216638	36(8, 29)–36(7, 30) A	440.48	146	1.53e−05	−5.1584	JPL
	$HCOOCH_3$	216830	18(2, 16)–17(2, 15) E	105.68	74	1.48e−04	−3.9849	JPL
	$HCOOCH_3$	216839	18(2, 16)–17(2, 15) A	105.67	74	1.48e−04	−3.9848	JPL
	$HCOOCH_3$	216963	20(0, 20)–19(1, 19) E	111.50	82	2.44e−05	−4.7309	JPL
	$HCOOCH_3$	216964	20(0, 20)–19(1, 19) A	111.48	82	2.44e−05	−4.7311	JPL
	$HCOOCH_3$	216965	20(1, 20)–19(1, 19) A	111.48	82	1.53e−04	−3.934	JPL
	$HCOOCH_3$	216966	20(1, 20)–19(1, 19) E	111.48	82	1.53e−04	−3.9341	JPL
	$HCOOCH_3$	216966	20(0, 20)–19(0, 19) E	111.50	82	1.53e−04	−3.9341	JPL
	$HCOOCH_3$	216967	20(0, 20)–19(0, 19) A	111.48	82	1.53e−04	−3.9339	JPL
	$HCOOCH_3$	216968	20(1, 20)–19(0, 19) E	111.50	82	2.44e−05	−4.7309	JPL
	$HCOOCH_3$	216969	20(1, 20)–19(0, 19) A	111.48	82	2.44e−05	−4.7311	JPL
	$HCOOCH_3$	217236	32(9, 24)–32(8, 25) E	367.80	130	1.59e−05	−5.0883	JPL
	$HCOOCH_3$	217263	37(10, 27)–37(9, 28) A	484.99	150	1.66e−05	−5.1787	JPL
	$HCOOCH_3$	218281	17(3, 14)–16(3, 13) E	99.73	70	1.51e−04	−3.9951	JPL
	$HCOOCH_3$	218298	17(3, 14)–16(3, 13)A	99.72	70	1.51e−04	−3.9949	JPL
	$HCOOCH_3$	218458	47(9, 38)–47(9, 39) A	738.69	190	5.61e−06	−5.916	JPL
	$HCOOCH_3$	218575	54(11, 43)–54(10, 44) A	978.10	218	1.87e−05	−5.6794	JPL
	$HCOOCH_3$	230316	22(9, 14)–22(8, 15) E	203.35	90	1.54e−05	−5.0498	JPL
	$HCOOCH_3$	230377	22(9, 14)–22(8, 15) A	203.36	90	1.61e−05	−5.0311	JPL
	$HCOOCH_3$	231232	29(4, 26)–29(3, 27) E	264.17	118	1.00e−05	−5.2074	JPL
	$HCOOCH_3$	231331	29(4, 26)–29(2, 27) A	264.16	118	5.25e−06	−5.4894	JPL
	$HCOOCH_3$	231457	40(7, 33)–40(6, 34) A	531.67	162	1.74e−05	−5.219	JPL
	$HCOOCH_3$	231470	35(10, 25)–35(9, 26) E	440.93	142	1.93e−05	−5.1005	JPL
	$HCOOCH_3$	231560	27(3, 25)–27(2, 26) E	221.72	110	7.22e−06	−5.3201	JPL
	$HCOOCH_3$	231561	27(3, 25)–27(1, 26) E	221.72	110	4.03e−06	−5.5734	JPL
	$HCOOCH_3$	232579	19(9, 11)–19(8, 12) E	165.96	78	1.53e−05	−5.0645	JPL
	$HCOOCH_3$	232597	19(9, 10)–19(8, 11) E	165.98	78	1.53e−05	−5.0647	JPL
	$HCOOCH_3$	233033	22(4, 18)–21(5, 17) E	165.28	90	8.19e−06	−5.274	JPL
	$HCOOCH_3$	233141	18(9, 9)–18(8, 10) E	154.73	74	1.49e−05	−5.0834	JPL
	$HCOOCH_3$	233213	19(4, 16)–18(4, 15) E	123.25	78	1.82e−04	−3.929	JPL
	$HCOOCH_3$	233213	19(17, 2)–18(17, 1) E	303.71	78	3.83e−05	−4.8663	JPL
	$HCOOCH_3$	233227	19(4, 16)–18(4, 15) A	123.24	78	1.82e−04	−3.9289	JPL
	$HCOOCH_3$	233247	19(16, 3)–18(16, 2) A	281.84	78	5.59e−05	−4.6708	JPL
	$HCOOCH_3$	233247	19(16, 4)–18(16, 3) A	281.84	78	5.59e−05	−4.6708	JPL
	$HCOOCH_3$	233310	19(15, 4)–18(15, 3) A	261.30	78	7.24e−05	−4.5287	JPL
	$HCOOCH_3$	233310	19(15, 5)–18(15, 4) A	261.30	78	7.24e−05	−4.5287	JPL
	$HCOOCH_3$	233395	19(14, 5)–18(14, 4) A	242.07	78	8.80e−05	−4.4167	JPL
	$HCOOCH_3$	233395	19(14, 6)–18(14, 5) A	242.07	78	8.80e−05	−4.4167	JPL
	$HCOOCH_3$	233397	19(14, 5)–18(14, 4) E	242.07	78	8.79e−05	−4.4168	JPL
	$HCOOCH_3$	233414	19(14, 6)–18(14, 5) E	242.06	78	8.80e−05	−4.4166	JPL
	$HCOOCH_3$	233505	19(13, 6)–18(13, 5) E	224.18	78	1.02e−04	−4.3248	JPL
	$HCOOCH_3$	233507	19(13, 6)–18(13, 5) A	224.18	78	1.02e−04	−4.3247	JPL
	$HCOOCH_3$	233507	19(13, 7)–18(13, 6) A	224.18	78	1.02e−04	−4.3247	JPL
	$HCOOCH_3$	233525	19(13, 7)–18(13, 6) E	224.17	78	1.03e−04	−4.3246	JPL
	$HCOOCH_3$	233598	17(9, 8)–17(8, 9) E	144.07	70	1.44e−05	−5.1069	JPL
	$HCOOCH_3$	233650	19(12, 7)–18(12, 6) E	207.61	78	1.16e−04	−4.2472	JPL
	$HCOOCH_3$	233655	19(12, 7)–18(12, 6) A	207.61	78	1.16e−04	−4.2472	JPL

Table C1
(Continued)

Name	Formula	f_{rest} (MHz)	Transition Number	E_u (K)	g_u	A_u (s^{-1})	$I_{CDMS.JPL}$	Reference
	$HCOOCH_3$	233655	19(12, 8)–18(12, 7) A	207.61	78	1.16e−04	−4.2472	JPL
	$HCOOCH_3$	233671	19(12, 8)–18(12, 7) E	207.60	78	1.16e−04	−4.2471	JPL
	$HCOOCH_3$	233754	18(4, 14)–17(4, 13) E	114.37	74	1.84e−04	−3.9352	JPL
	$HCOOCH_3$	233778	18(4, 14)–17(4, 13) A	114.36	74	1.84e−04	−3.9351	JPL
	$HCOOCH_3$	233845	19(11, 8)–18(11, 7) E	192.39	78	1.29e−04	−4.1808	JPL
	$HCOOCH_3$	233854	19(11, 8)–18(11, 7) A	192.38	78	1.29e−04	−4.1807	JPL
	$HCOOCH_3$	233854	19(11, 9)–18(11, 8) A	192.38	78	1.29e−04	−4.1807	JPL
	$HCOOCH_3$	233867	19(11, 9)–18(11, 8) E	192.37	78	1.29e−04	−4.1807	JPL
Silicon monoxide	SiO	217105	5–4	31.26	11	5.21e−04	−1.3166	JPL
Sulfur dioxide	SO_2	216643	22(2, 20)–22(1, 21)	248.44	45	9.27e−05	−3.0823	JPL
Sulfur monoxide (^{34}S-substituted)	^{34}SO	215840	6(5)–5(4)	34.38	13	1.26e−04	−2.3335	JPL

Note. The f_{rest} is the rest frequency in MHz, E_u is the energy of the upper state in K, g_u is the degeneracy factor, A_u is the Einstein A coefficient in s^{-1}, $I_{CDMS,JPL}$ is the CDMS/JPL intensity, and the transition number is in the form of upper state–lower state.

References. Jet Propulsion Laboratory Molecular Spectroscopy (JPL, Pickett et al. 1998), Cologne Database for Molecular Spectroscopy (CDMS, Müller et al. 2005), eXtended CASA Line Analysis Software Suite (XCLASS, Möller et al. 2017).

Appendix D
Population Diagram of Methanol

The population diagram method is also a common tool for analyzing the excitation of molecular emission (Goldsmith & Langer 1999). In this section, we show the population diagrams of CH_3OH in all four sources (Figure D1). We have excluded from the analysis the transition $J(K_a, K_c) = 4$ (2,2)–3(1,2) E ($f_{\rm rest} = 218{,}440$ MHz; $E_u = 45$ K) because it has been reported to be possibly masing in different astrophysical objects (Hunter et al. 2014; Leurini et al. 2016; Yuan et al. 2018).

The total column density ($N_{\rm tot}$) and the rotational temperature derived from the rotational diagrams are in general consistent with the MAGIX results (see Section 3.2). The data points in G208 at lower (<200 K) and higher (>200 K) energy levels seem to have different slopes. This could indicate the possibility of multiple molecular emission components in different excitation temperatures (e.g., cold envelope and hot corino).

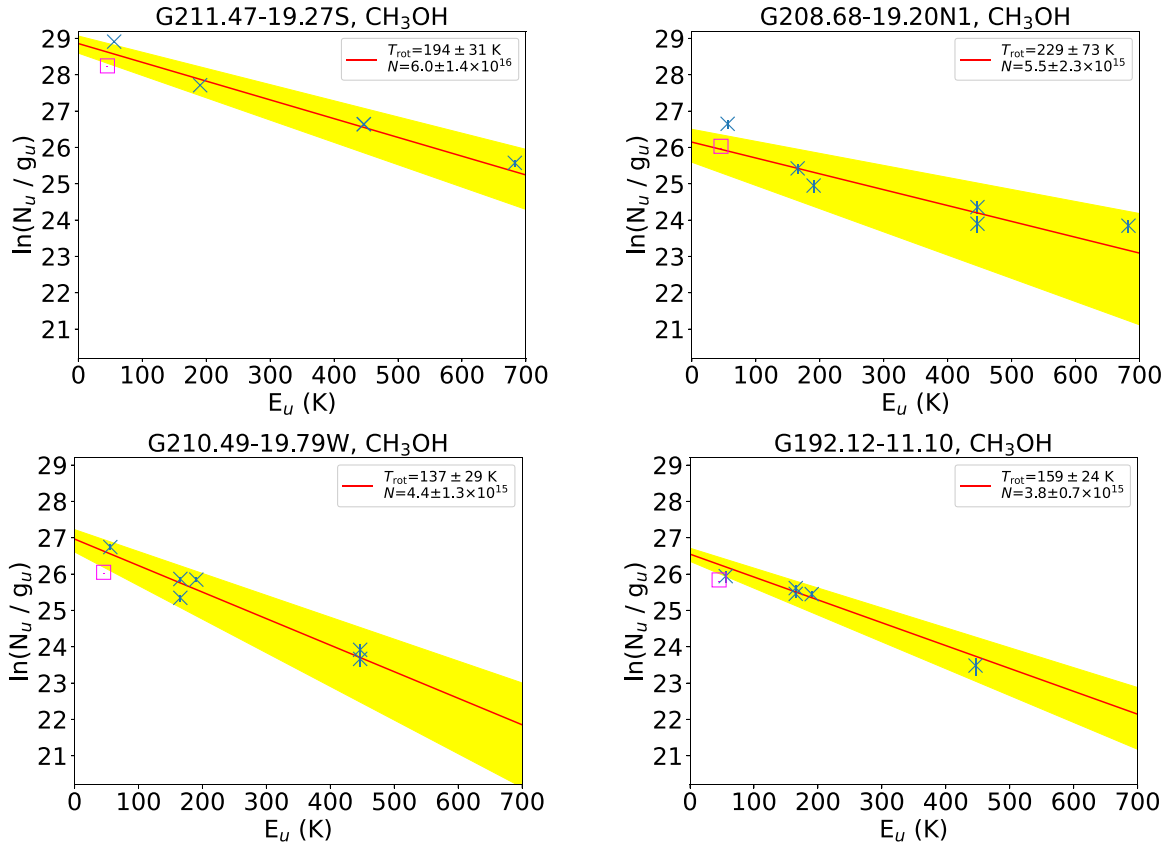

Figure D1. Rotational diagrams (RD) of CH_3OH. The red line shows the best-fit result from the RD analysis, and the yellow area represents the 1σ interval. We adopted the molecular parameters, including the partition function, from the Cologne Database for Molecular Spectroscopy (CDMS, Müller et al. 2005). The magenta squares mark the transition $J(K_a, K_c) = 4(2,2)$–$3(1,2)$ E, which is not used in the fitting.

ORCID iDs

Shih-Ying Hsu https://orcid.org/0000-0002-1369-1563
Sheng-Yuan Liu https://orcid.org/0000-0003-4603-7119
Tie Liu https://orcid.org/0000-0002-5286-2564
Dipen Sahu https://orcid.org/0000-0002-4393-3463
Naomi Hirano https://orcid.org/0000-0001-9304-7884
Chin-Fei Lee https://orcid.org/0000-0002-3024-5864
Ken'ichi Tatematsu https://orcid.org/0000-0002-8149-8546
Gwanjeong Kim https://orcid.org/0000-0003-2011-8172
Mika Juvela https://orcid.org/0000-0002-5809-4834
Patricio Sanhueza https://orcid.org/0000-0002-7125-7685
Jinhua He https://orcid.org/0000-0002-3938-4393
Doug Johnstone https://orcid.org/0000-0002-6773-459X
Sheng-Li Qin https://orcid.org/0000-0003-2302-0613
Leonardo Bronfman https://orcid.org/0000-0002-9574-8454
Huei-Ru Vivien Chen https://orcid.org/0000-0002-9774-1846
Somnath Dutta https://orcid.org/0000-0002-2338-4583
David J. Eden https://orcid.org/0000-0002-5881-3229
Kai-Syun Jhan https://orcid.org/0000-0003-2069-1403
Kee-Tae Kim https://orcid.org/0000-0003-2412-7092
Yi-Jehng Kuan https://orcid.org/0000-0002-4336-0730
Woojin Kwon https://orcid.org/0000-0003-4022-4132
Chang Won Lee https://orcid.org/0000-0002-3179-6334
Jeong-Eun Lee https://orcid.org/0000-0003-3119-2087
M. G. Rawlings https://orcid.org/0000-0002-6529-202X
Hsien Shang https://orcid.org/0000-0001-8385-9838
Archana Soam https://orcid.org/0000-0002-6386-2906
Alessio Traficante https://orcid.org/0000-0003-1665-6402
Yuefang Wu https://orcid.org/0000-0002-5076-7520
Yao-Lun Yang https://orcid.org/0000-0001-8227-2816
Qizhou Zhang https://orcid.org/0000-0003-2384-6589

References

Araki, M., Takano, S., Sakai, N., et al. 2016, ApJ, 833, 291
Araya, E., Hofner, P., Kurtz, S., Olmi, L., & Linz, H. 2008, ApJ, 675, 420
Astropy Collaboration, Robitaille, T. P., Tollerud, E. J., et al. 2013, A&A, 558, A33
Barone, V., Latouche, C., Skouteris, D., et al. 2015, MNRAS, 453, L31
Beckwith, S. V. W., Sargent, A. I., Chini, R. S., & Guesten, R. 1990, AJ, 99, 924
Belloche, A., Maury, A. J., Maret, S., et al. 2020, A&A, 635, 198
Bergner, J. B., Martín-Doménech, R., Öberg, K. I., et al. 2019, ESC, 3, 1564
Bianchi, E., Codella, C., Ceccarelli, C., et al. 2017, MNRAS, 467, 3011
Bianchi, E., Codella, C., Ceccarelli, C., et al. 2018, MNRAS, 483, 1850
Bottinelli, S., Ceccarelli, C., Lefloch, B., et al. 2004, ApJ, 615, 354
Bottinelli, S., Ceccarelli, C., Williams, J. P., & Lefloch, B. 2007, A&A, 463, 601
Cazaux, S., Tielens, A. G. G. M., Ceccarelli, C., et al. 2003, ApJL, 593, L51
Ceccarelli, C. 2004, in ASP Conf. Proc. 323, Star Formation in the Interstellar Medium: In Honor of David Hollenbach, Chris McKee and Frank Shu, ed. D. L. D. N. D. Johnstone, F. C. Adams, & E. Ostriker (San Francisco, CA: ASP), 195
Chini, R., Reipurth, B., Ward-Thompson, D., et al. 1997, ApJL, 474, L135
Codella, C., Ceccarelli, C., Cabrit, S., et al. 2016, A&A, 586, L3
Drozdovskaya, M. N., van Dishoeck, E. F., Jørgensen, J. K., et al. 2018, MNRAS, 476, 4949
Eden, D. J., Liu, T., Kim, K.-T., et al. 2019, MNRAS, 485, 2895
Esplugues, G. B., Viti, S., Goicoechea, J. R., & Cernicharo, J. 2014, A&A, 567, A95
Evans, N. J., Francesco, J. D., Lee, J.-E., et al. 2015, ApJ, 814, 22
Fang, M., Kim, J. S., van Boekel, R., et al. 2013, ApJS, 207, 5
Fischer, W. J., Megeath, S. T., Ali, B., et al. 2010, A&A, 518, L122
Friberg, P., Madden, S. C., Hjalmarson, A., & Irvine, W. M. 1988, A&A, 195, 281
Furlan, E., Fischer, W. J., Ali, B., et al. 2016, ApJS, 224, 5
Garrod, R. T., Weaver, S. L. W., & Herbst, E. 2008, ApJ, 682, 283
Goldsmith, P. F., & Langer, W. D. 1999, ApJ, 517, 209
Halfen, D. T., Ilyushin, V., & Ziurys, L. M. 2011, ApJ, 743, 60
Hatchell, J., Thompson, M. A., Millar, T. J., & MacDonald, G. H. 1998, A&A, 338, 713
Herbst, E., & van Dishoeck, E. F. 2009, ARA&A, 47, 427
Higuchi, A. E., Sakai, N., Watanabe, Y., et al. 2018, ApJS, 236, 52
Hirano, N., & Liu, F.-C. 2014, ApJ, 789, 50
Hunter, T. R., Brogan, C. L., Cyganowski, C. J., & Young, K. H. 2014, ApJ, 788, 187
Imai, M., Sakai, N., Oya, Y., et al. 2016, ApJL, 830, L37
Jacobsen, S. K., Jørgensen, J. K., Francesco, J. D., et al. 2019, A&A, 629, A29
Jones, B. M., Bennett, C. J., & Kaiser, R. I. 2011, ApJ, 734, 78
Jorgensen, J. K., Bourke, T. L., Myers, P. C., et al. 2005, ApJ, 632, 973
Jørgensen, J. K., Müller, H. S. P., Calcutt, H., et al. 2018, A&A, 620, A170
Jørgensen, J. K., van der Wiel, M. H. D., Coutens, A., et al. 2016, A&A, 595, A117
Juvela, M., He, J., Pattle, K., et al. 2018, A&A, 612, A71
Kauffmann, J., Bertoldi, F., Bourke, T. L., Evans, N. J., & Lee, C. W. 2008, A&A, 487, 993
Le Gal, R., Öberg, K. I., Loomis, R. A., Pegues, J., & Bergner, J. B. 2019, ApJ, 876, 72
Lee, C.-F., Codella, C., Li, Z.-Y., & Liu, S.-Y. 2019, ApJ, 876, 63
Lee, C.-F., Li, Z.-Y., Ho, P. T. P., et al. 2017, ApJ, 843, 27
Lefloch, B., Bachiller, R., Ceccarelli, C., et al. 2018, MNRAS, 477, 4792
Leurini, S., Menten, K. M., & Walmsley, C. M. 2016, A&A, 592, A31
Liu, T., Kim, K.-T., Juvela, M., et al. 2018, ApJS, 234, 28
López-Sepulcre, A., Jaber, A. A., Mendoza, E., et al. 2015, MNRAS, 449, 2438
López-Sepulcre, A., Sakai, N., Neri, R., et al. 2017, A&A, 606, A121
Luo, G., Feng, S., Li, D., et al. 2019, ApJ, 885, 82
Manoj, P., Green, J. D., Megeath, S. T., et al. 2016, ApJ, 831, 69
Manoj, P., Watson, D. M., Neufeld, D. A., et al. 2013, ApJ, 763, 83
Martín-Doménech, R., Bergner, J. B., Öberg, K. I., & Jørgensen, J. K. 2019, ApJ, 880, 130
Martin-Domenech, R., Oberg, K. I., & Rajappan, M. 2020, ApJ, 894, 98
McMullin, J. P., Waters, B., Schiebel, D., Young, W., & Golap, K. 2007, in ASP Conf. Ser. 376, Astronomical Data Analysis Software and Systems XVI, ed. R. A. Shaw, F. Hill, & D. J. Bell (San Francisco, CA: ASP), 127
Megeath, S. T., Gutermuth, R., Muzerolle, J., et al. 2012, AJ, 144, 192
Möller, T., Bernst, I., Panoglou, D., et al. 2013, A&A, 549, A21
Möller, T., Endres, C., & Schilke, P. 2017, A&A, 598, A7
Müller, H. S., Schlöder, F., Stutzki, J., & Winnewisser, G. 2005, JMoSt, 742, 215
Noble, J. A., Theule, P., Congiu, E., et al. 2015, A&A, 576, A91
Ospina-Zamudio, J., Lefloch, B., Ceccarelli, C., et al. 2018, A&A, 618, A145
Oya, Y., Sakai, N., Watanabe, Y., et al. 2017, ApJ, 837, 174
Palumbo, M. E., Geballe, T. R., & Tielens, A. G. G. M. 1997, ApJ, 479, 839
Parise, B., Ceccarelli, C., Tielens, A. G. G. M., et al. 2006, A&A, 453, 949
Persson, M. V., Jørgensen, J. K., Müller, H. S. P., et al. 2018, A&A, 610, A54
Pickett, H., Poynter, R., Cohen, E., et al. 1998, JQSRT, 60, 883
Planck Collaboration, Ade, P. A. R., Agnahim, N., et al. 2016, A&A, 594, A28
Price-Whelan, A. M., Sipőcz, B. M., Günther, H. M., et al. 2018, AJ, 156, 123
Quan, D., & Herbst, E. 2007, A&A, 474, 521
Raunier, S., Chiavassa, T., Duvernay, F., et al. 2004, A&A, 416, 165
Roberts, H., & Millar, T. J. 2000, A&A, 361, 388
Sahu, D., Liu, S.-Y., Su, Y.-N., et al. 2019, ApJ, 872, 196
Sakai, N., Sakai, T., Hirota, T., Burton, M., & Yamamoto, S. 2009, ApJ, 697, 769
Sakai, N., Sakai, T., Hirota, T., & Yamamoto, S. 2008, ApJ, 672, 371
Saladino, R., Botta, G., Pino, S., Costanzo, G., & Di Mauro, E. 2012, Chem. Soc. Rev., 41, 5526
Sanhueza, P., Jackson, J. M., Foster, J. B., et al. 2013, ApJ, 773, 123
Takahashi, S., & Ho, P. T. P. 2012, ApJL, 745, L10
Takahashi, S., Machida, M. N., Tomisaka, K., et al. 2019, ApJ, 872, 70
Taquet, V., Charnley, S. B., & Sipilä, O. 2014, ApJ, 791, 1
Taquet, V., López-Sepulcre, A., Ceccarelli, C., et al. 2015, ApJ, 804, 81
Tatematsu, K., Liu, T., Ohashi, S., et al. 2017, ApJS, 228, 12
Tobin, J. J., Megeath, S. T., van't Hoff, M., et al. 2019, ApJ, 886, 6
van Kempen, T. A., Hogerheijde, M. R., van Dishoeck, E. F., et al. 2016, A&A, 587, A17
Velusamy, T., Langer, W. D., & Thompson, T. 2014, ApJ, 783, 6
Watson, D. M., Calvet, N. P., Fischer, W. J., et al. 2016, ApJ, 828, 52
Wenger, M., Ochsenbein, F., Egret, D., et al. 2000, A&AS, 143, 9
Wirström, E. S., Geppert, W. D., Hjalmarson, Å., et al. 2011, A&A, 533, A24
Yang, Y.-L., Evans, N. J., Smith, I., et al. 2020, ApJ, 891, 61
Yi, H.-W., Lee, J.-E., Liu, T., et al. 2018, ApJS, 236, 51
Yuan, J., Li, J.-Z., Wu, Y., et al. 2018, ApJ, 852, 12